Draft version January 31, 2017
Preprint typeset using LaTeX style AASTeX6 v. 1.0

CONSISTENT SPH SIMULATIONS OF PROTOSTELLAR COLLAPSE AND FRAGMENTATION

Ruslan Gabbasov
Instituto de Ciencias Básicas e Ingenierías, Universidad Autónoma del Estado de Hidalgo (UAEH),
Ciudad Universitaria, Carretera Pachuca-Tulacingo km. 4.5 S/N, Colonia Carboneras,
Mineral de la Reforma, C.P. 42184, Hidalgo, Mexico

Leonardo Di G. Sigalotti, Fidel Cruz
Área de Física de Procesos Irreversibles, Departamento de Ciencias Básicas,
Universidad Autónoma Metropolitana-Azcapotzalco (UAM-A), Av. San Pablo 180,
C.P. 02200, Ciudad de México, Mexico

Jaime Klapp[1]
Departamento de Física, Instituto Nacional de Investigaciones Nucleares (ININ),
Carretera México-Toluca km. 36.5, La Marquesa, 52750 Ocoyoacac, Estado de México, Mexico

José M. Ramírez-Velasquez[1]
Centro de Física, Instituto Venezolano de Investigaciones Científicas (IVIC),
Apartado Postal 20632, Caracas 1020A, Venezuela

[1]ABACUS-Centro de Matemáticas Aplicadas y Cómputo de Alto Rendimiento,
Departamento de Matemáticas, Centro de Investigación y de Estudios Avanzados (Cinvestav-IPN),
Carretera México-Toluca km. 38.5, La Marquesa, 52740 Ocoyoacac, Estado de México, Mexico

ABSTRACT

We study the consistency and convergence of smoothed particle hydrodynamics (SPH), as a function of the interpolation parameters, namely the number of particles N, the number of neighbors n, and the smoothing length h, using simulations of the collapse and fragmentation of protostellar rotating cores. The calculations are made using a modified version of the GADGET-2 code that employs an improved scheme for the artificial viscosity and power-law dependences of n and h on N, as was recently proposed by Zhu et al., which comply with the combined limit $N \to \infty$, $h \to 0$, and $n \to \infty$ with $n/N \to 0$ for full SPH consistency, as the domain resolution is increased. We apply this realization to the "standard isothermal test case" in the variant calculated by Burkert & Bodenheimer and the Gaussian cloud model of Boss to investigate the response of the method to adaptive smoothing lengths in the presence of large density and pressure gradients. The degree of consistency is measured by tracking how well the estimates of the consistency integral relations reproduce their continuous counterparts. In particular, C^0 and C^1 particle consistency is demonstrated, meaning that the calculations are close to second-order accuracy. **As long as n is increased with N, mass resolution also improves as the minimum resolvable mass $M_{\rm min} \sim n^{-1}$. This aspect allows proper calculation of small-scale structures in the flow associated with the formation and instability of protostellar disks around the growing fragments, which are seen to develop a spiral structure and fragment into close binary/multiple systems as supported by recent observations**.

Keywords: Hydrodynamics — Methods: numerical — Stars: formation — Binaries: general

1. INTRODUCTION

The method of smoothed particle hydrodynamics (SPH) was developed in the late 1970s by Gingold & Monaghan (1977) and Lucy (1977) as a numerical tool for solving the equations of gravitohydrodynamics in three-dimensional

open space. Today, the use of SPH spans many areas of astrophysics and cosmology as well as a broad range of fluid and solid mechanics related areas. However, despite its extensive applications and recent progress in consolidating its theoretical foundations, SPH still has unknown properties that need to be investigated. A fundamental numerical aspect of SPH is the lack of particle consistency, which affects the accuracy and convergence of the method. Several modified techniques and corrective methods have been proposed to restore particle consistency in fluid dynamics calculations (Li & Liu 1996; Bonet & Lok 1999; Chen et al. 1999; Liu et al. 2003; Zhang & Batra 2004; Liu & Liu 2006; Sibilla 2015); the most successful ones being those based on Taylor series expansions of the kernel approximations of a function and its derivatives. If m derivatives are retained in the series expansions, the resulting kernel and particle approximations will have $(m+1)$th-order accuracy or C^m consistency. However, the improved accuracy of these methods comes at the price of involving matrix inversions, which represent a major computational burden for time-evolving simulations and eventually a loss of numerical stability due to matrix conditioning for some specific problems. On the other hand, while these corrective methods solve for particle inconsistency due to truncation of the kernel at model boundaries, it is not clear how irregular particle distributions and the use of variable smoothing lengths affect the consistency (and therefore the accuracy) of the solutions. Recently, Litvinov et al. (2015) showed that the condition for the particle approximation to restore C^0 consistency and achieve asymptotic error decay is that the volumes defined by the particles and the inter-particle faces partition the entire domain, i.e., constitute a partition of unity. They found that this condition is satisfied by relaxing the particles under a constant pressure field by keeping the particle volumes invariant, yielding convergence rates for such a relaxed distribution that are the same as those for particles on a perfect regular lattice. Quite curiously, they also observed that the relaxed particle distributions obtained this way resemble that of liquid molecules resulting from microscopic simulations. A method to improve the SPH estimate of derivatives which is not affected by particle disorder was also devised recently by Sibilla (2015).

In comparison little work has been done to improve the SPH consistency in astrophysical applications. In many cases, especially those involving self-gravitating flows, large density gradients arise and an adaptive kernel is used to guarantee spatial resolution in regions of high density. It has long been recognized that spatially adaptive calculations where a variable smoothing length is employed turn out to be inconsistent (Liu & Liu 2006). It was not until recently that Zhu et al. (2015) identified another source of particle inconsistency associated with the finite number of neighbors within the compact support of a smoothed function. It is common practice in SPH calculations to assume that a large number of total particles, N, and a small smoothing length, h, are sufficient conditions to achieve consistent solutions, while holding the number of neighbor particles, n, fixed at some value $n \ll N$. Zhu et al. (2015) demonstrated that C^0 particle consistency, i.e., satisfaction of the discrete normalization condition of the kernel function can only be achieved when n is sufficiently large for which the finite SPH sum approximation approaches the continuous limit. This result is consistent with the error analysis of the SPH representation of the continuity and momentum equations carried out by Read et al. (2010), who found that particle consistency is completely lost due to zeroth-order error terms that would persist when working with a finite number of neighbors even though $N \to \infty$ and $h \to 0$. Indeed, as the resolution is increased, approaching the limit $N \to \infty$ and $h \to 0$, the overall error will grow at a faster rate if the magnitude of the zeroth-order error terms remains constant. Based on these observations, full particle consistency is possible in SPH only if the joint limit $N \to \infty$, $h \to 0$, and $n \to \infty$ is satisfied (Zhu et al. 2015). However, we recall that this combined limit was first noted by Rasio (2000) using a simple linear analysis on one-dimensional sound wave propagation. In particular, he found that SPH is fully consistent in this limit with $N \to \infty$ faster than n such that $n/N \to 0$.

On the other hand, Monaghan (1992) conjectured that for quasi-regularly distributed particles, the discretization error made when passing from the continuous kernel to the particle approximation is proportional to $(\log n)^d/n$, where d is the dimension. For $n \gg 1$, Zhu et al. (2015) parameterized this error as $\sim n^{-\gamma}$, where γ varies from 0.5 for a random distribution to 1 for a perfectly regular lattice of particles. Combining this with the leading error ($\propto h^2$) of the continuous kernel approximation for most commonly used kernel forms, Zhu et al. (2015) derived the scaling relations $n \propto N^{1/2}$ and $h \propto N^{-1/6}$, which satisfy the joint limit as the domain resolution is progressively increased. A recent analysis on standard SPH has demonstrated that using the above scalings C^0 consistency is fully restored for both the estimates of the function and its derivatives in contrast to the case where n is fixed to a constant small value, with the numerical solution becoming also insensitive to the degree of particle disorder (Sigalotti et al. 2016).

While these results are promising, it remains to investigate the response of the method for spatially adaptive calculations in the presence of large gradients where the loss of particle consistency is known to be most extreme. In particular, most of the above analyses are based on static convergence tests for analytical functions in two- or three-space dimensions using either uniformly or irregularly distributed point sets, or on dynamical test problems for which an analytical solution is known in advance, and therefore the results obtained are limited to idealized circumstances. As

was emphasized by Zhu et al. (2015), the lack of consistency associated with particle disorder and spatial adaptivity is not specific to a particular SPH scheme but is rather a generic problem. It would therefore be desirable to test the present method for more complex models as those involving the solution of the equations of hydrodynamics coupled to gravity in three-space dimensions. To do so we choose as a problem the gravitational collapse and fragmentation of an initially rotating protostellar cloud, using a modified version of the GADGET-2 code (Springel 2005). As templates for the model clouds we use the "standard isothermal test case" in the variant calculated by Burkert & Bodenheimer (1993) and the centrally condensed, Gaussian cloud model of Boss (1991) coupled to a barotropic equation of state to mimic the nonisothermal collapse. The simulations will then allow to better understand the impact of varying the number of neighbors as the resolution is increased on the SPH discretization errors, which will naturally emerge from the density estimate itself and the SPH momentum equation. The convergence and accuracy of the simulations is measured by evaluating how well the particle approximation of the integral consistency relations (or moments of the kernel) are satisfied during the evolution.

A further implication of the consistency scaling relations on protostellar collapse calculations is the improved mass resolution. Since the minimum resolvable mass, $M_{\rm min}$, scales with h as h^3, this implies that $M_{\rm min} \sim n^{-1}$. Although the collapse models proposed here start from ideal conditions, this aspect has an important impact on the outcome of the simulations, where well-defined, rotating circumstellar disks are seen to form around the growing fragments, which then increase in mass, develop spiral arms, and fragment to produce small-scale binary/multiple protostellar systems. This result is consistent with recent observations of L1448 IRS3B (Tobin et al. 2016): a close triple protostar system where two of the protostars formed by fragmentation of a massive disk with a spiral structure surrounding a primary, young star formed from the collapse of a larger cloud of gas and dust. While based principally on the relative proximity of the companion stars, this observation provides for the first time direct evidence of protostellar disk fragmentation as a mechanism for the formation of close binary/multiple young stars.

2. THE ISSUE OF CONSISTENCY

We start by recalling that the kernel (or smoothed) estimate of a scalar function $f(\mathbf{r})$, where f may be either the density, ρ, or the gas pressure, p, is defined by

$$\langle f(\mathbf{r})\rangle = \int_{\mathcal{R}^3} f(\mathbf{r}')W(|\mathbf{r}-\mathbf{r}'|,h)d^3\mathbf{r}', \tag{1}$$

where the volume integration is taken over the whole real space, $\mathbf{r}=(x,y,z)$ denotes position, and W is the kernel interpolation function, which must be positive definite, symmetric, monotonically decreasing, and satisfy the normalization condition

$$\int_{\mathcal{R}^3} W(|\mathbf{r}-\mathbf{r}'|,h)d^3\mathbf{r}' = 1, \tag{2}$$

together with the Dirac-δ function property that is observed when $h\to 0$. Moreover, suitable kernels should have a compact support so that $W(|\mathbf{r}-\mathbf{r}'|,h)=0$ for $|\mathbf{r}-\mathbf{r}'|\geq kh$, where k is some integer that depends on the kernel function itself. Making the change of variable $|\mathbf{r}-\mathbf{r}'|\to h|\mathbf{r}-\mathbf{r}'|$, it is easy to show that the following scaling relation holds (Sigalotti et al. 2016)

$$W(h|\mathbf{r}-\mathbf{r}'|,h) = \frac{1}{h^\nu}W(|\mathbf{r}-\mathbf{r}'|,1), \tag{3}$$

for any SPH kernel function, where $\nu = 1$, 2, and 3 in one-, two-, and three-space dimensions, respectively.

If we expand in Taylor series $f(\mathbf{r}')$ around $\mathbf{r}'=\mathbf{r}$, make $\mathbf{r}\to h\mathbf{r}$ and $\mathbf{r}'\to h\mathbf{r}'$, use Eq. (3), and insert the result in the kernel approximation (1), we obtain for the function estimate the relation

$$\langle f(h\mathbf{r})\rangle = \sum_{l=0}^{\infty}\frac{h^l}{l!}\nabla_h^{(l)}f(h\mathbf{r}) ::: \cdots : \int_{\mathcal{R}^3}(\mathbf{r}'-\mathbf{r})^l W(|\mathbf{r}-\mathbf{r}'|,1)d^3\mathbf{r}', \tag{4}$$

where $\nabla_h^{(l)}$ denotes the product of the ∇ operator with respect to coordinates (hx,hy,hz) l times, $(\mathbf{r}'-\mathbf{r})^l$ is a tensor of rank l, and the symbol "$::: \cdots :$" is used to denote the lth-order inner product. Therefore, if the kernel approximation is to exactly reproduce a sufficiently smooth function to $(m+1)$th order, the family of consistency relations must be fulfilled

$$M_0 = \int_{\mathcal{R}^3} W(|\mathbf{r}-\mathbf{r}'|,1)d^3\mathbf{r}' = 1, \tag{5}$$

$$\mathbf{M}_l = \int_{\mathcal{R}^3} (\mathbf{r}' - \mathbf{r})^l W(|\mathbf{r} - \mathbf{r}'|, 1) d^3\mathbf{r}' = \mathbf{0}^{(l)}, \qquad \text{for} \qquad l = 1, 2, ..., m, \tag{6}$$

where $\mathbf{0}^{(1)} = \mathbf{0} = (0, 0, 0)$ is the null vector and $\mathbf{0}^{(l)}$ is the zero tensor of rank l. Fulfillment of the integral relations (5) and (6) guarantees C^m consistency for the kernel estimate of the function, which by virtue of Eq. (4) reproduces exactly the continuous function to order $m + 1$. Owing to the scaling relation (3), the contribution of the error due to the smoothing length can be separated from that due to the discrete representation of the integral, which, being independent of h, will only depend on the number of neighbors within the kernel support and their spatial distribution.

When solving the gravitohydrodynamics equations, gas compression is accounted for by evaluating the pressure gradient in the momentum equation. Therefore, consistency relations for the kernel estimate of the gradient of a function are also of concern. Using the definition of the kernel estimate of the gradient as

$$\langle \nabla f(\mathbf{r}) \rangle = \int_{\mathcal{R}^3} f(\mathbf{r}') \nabla W(|\mathbf{r} - \mathbf{r}'|, h) d^3\mathbf{r}', \tag{7}$$

expanding $f(\mathbf{r}')$ again in Taylor series about $\mathbf{r}' = \mathbf{r}$, making $\mathbf{r} \to h\mathbf{r}$ and $\mathbf{r}' \to h\mathbf{r}'$, and inserting the result in Eq. (7) we obtain the form

$$\langle \nabla_h f(h\mathbf{r}) \rangle = \sum_{l=0}^{\infty} \frac{h^{l-1}}{l!} \nabla_h^{(l)} f(h\mathbf{r}) \,\vdots\vdots\, \cdots : \int_{\mathcal{R}^3} (\mathbf{r}' - \mathbf{r})^l \nabla W(|\mathbf{r} - \mathbf{r}'|, 1) d^3\mathbf{r}', \tag{8}$$

where we have made use of the scaling relation

$$\nabla W(h|\mathbf{r} - \mathbf{r}'|, h) = \frac{1}{h^\nu} \nabla W(|\mathbf{r} - \mathbf{r}'|, 1), \tag{9}$$

with $\nu = 3$, which also holds for the gradient of the kernel. From Eq. (8), it follows that C^m consistency for the kernel estimate of the gradient is obtained only if the family of integral relations is exactly satisfied

$$\mathbf{M}'_0 = \int_{\mathcal{R}^3} \nabla W(|\mathbf{r} - \mathbf{r}'|, 1) d^3\mathbf{r}' = \int_{\mathcal{R}^2} W(|\mathbf{r} - \mathbf{r}'|, 1) \mathbf{n} d^2\mathbf{r}' = \mathbf{0}, \tag{10}$$

$$\mathbf{M}'_1 = \int_{\mathcal{R}^3} (\mathbf{r}' - \mathbf{r}) \nabla W(|\mathbf{r} - \mathbf{r}'|, 1) d^3\mathbf{r}' = \mathbf{I}, \tag{11}$$

$$\mathbf{M}'_l = \int_{\mathcal{R}^3} (\mathbf{r}' - \mathbf{r})^l \nabla W(|\mathbf{r} - \mathbf{r}'|, 1) d^3\mathbf{r}' = \mathbf{0}^{(l+1)}, \qquad \text{for} \qquad l = 2, 3, ..., m, \tag{12}$$

where $\mathbf{I}$ is the unit tensor. The second equality in Eq. (10) holds for any volume enclosed by a continuous surface with differential volume element $d^3\mathbf{r}'$ and differential surface element $\mathbf{n}d^2\mathbf{r}'$, where $\mathbf{n}$ is the outward unit normal from the volume surface. It is precisely the requirement that the zeroth moment $\mathbf{M}'_0 = \mathbf{0}$, which determines that the surface integral of the kernel must vanish identically. Because of the symmetry of the kernel function, relations (5) and (6) with l odd are automatically satisfied, while those with l even will all appear in the expansion (4) as finite sources of error and will not vanish unless the kernel approaches the Dirac-δ distribution. Hence, up to leading second-order Eq. (4) becomes

$$\langle f(h\mathbf{r}) \rangle = f(h\mathbf{r}) + \frac{1}{2} h^2 \nabla_h \nabla_h f(h\mathbf{r}) : \int_{\mathcal{R}^3} (\mathbf{r}' - \mathbf{r})^2 W(|\mathbf{r} - \mathbf{r}'|, 1) d^3\mathbf{r}' + O(h^4), \tag{13}$$

which expresses that the kernel approximation of a function has C^1 consistency for an unbounded domain. Using Eq. (1) it is a simple matter to show that the integral on the right-hand side of Eq. (13), which corresponds to the second moment of the kernel $\mathbf{M}_2$, is equal to $\langle \mathbf{rr} \rangle - \langle \mathbf{r} \rangle \langle \mathbf{r} \rangle \neq \mathbf{0}^{(2)}$, implying that C^2 consistency is not achieved even though C^0 and C^1 consistencies are automatically satisfied (Sigalotti et al. 2016). This term is just the variance of the particle position vector $\mathbf{r}$ and is a measure of the spread of the particle positions relative to the mean. Evidently, $\langle \mathbf{rr} \rangle - \langle \mathbf{r} \rangle \langle \mathbf{r} \rangle \to \mathbf{0}^{(2)}$ only when $W(|\mathbf{r} - \mathbf{r}'|, 1) \to \delta(\mathbf{r} - \mathbf{r}')$, or equivalently, when $N \to \infty$, $h \to 0$, and $n \to \infty$.

Similarly, due to the symmetry of the kernel all integrals in Eqs. (10)-(12) will vanish identically for l even, while only those for l odd will survive in the series expansion (8), which up to second-order becomes

$$\langle \nabla_h f(h\mathbf{r}) \rangle = \nabla_h f(h\mathbf{r}) + \frac{1}{6} h^2 \nabla_h \nabla_h \nabla_h f(h\mathbf{r}) \vdots \int_{\mathcal{R}^3} (\mathbf{r}' - \mathbf{r})^3 \nabla W(|\mathbf{r} - \mathbf{r}'|, 1) d^3\mathbf{r}' + O(h^4), \tag{14}$$

where the symbol "$\vdots$" is used to denote the triple inner product. Note that the integral on the right-hand side of Eq. (14) is the third moment of the kernel gradient $\mathbf{M}'_3 = 3\mathbf{M}_2\mathbf{I} \neq \mathbf{0}^{(4)}$. We recall that relations (5) and (11) have important physical implications. In particular, satisfaction of relation (5) means that the homogeneity of space is not

affected by the SPH kernel approximation, which has as a consequence the conservation of linear momentum. On the other hand, fulfillment of relation (11) expresses that the isotropy of space is preserved by the kernel approximation, and therefore angular momentum is locally conserved (Vignjevic 2009; Sigalotti et al. 2016).

An important feature of Eqs. (13) and (14) is that the contribution of h to the error can be separated from the error carried by the discretization of the consistency relations, which will only depend on the number of neighbors, n, and how they are distributed within the kernel support. In general, it is well-known that the particle approximation of Eq. (5) diverges from being exactly one, i.e.,

$$M_{0,a} = \sum_{b=1}^{n} W_{ab}\Delta V_b \neq 1, \tag{15}$$

where $W_{ab} = W(|\mathbf{r}_a - \mathbf{r}_b|, h)$ and ΔV_b is the volume of the subdomain of neighbor particle b. The error carried by Eq. (15) scales as $\sim n^{-\gamma}$, with $\gamma \in [0.5, 1]$, depending on the particle distribution (Monaghan 1992; Zhu et al. 2015). Therefore, as the number of neighbors is increased the discrete normalization condition approaches unity and C^0 particle consistency is restored. This will also make the particle approximations of relations (10) and (11) to approach the null vector $\mathbf{0}$ and the unit tensor, respectively. These conditions state that the particles should provide a good approximation to a partition of unity. As in traditional finite difference and finite element methods, the concept of consistency in SPH defines how well the discrete model equations represent the exact equations in the continuum limit. In SPH this is accomplished in two separate steps: the kernel approximation which, as we have described above, is derived from the continuous form, and the particle approximation, where the integrals are replaced by sums over a finite set of particles within the kernel support. Since the kernel consistency relations do not assure consistency for the particle approximation, the discrete counterparts of Eqs. (13) and (14) must be written as

$$f_a \to \langle f\rangle_a = M_{0,a}(f)_a + h(\nabla f)_a \cdot \mathbf{M}_{1,a} + \frac{1}{2}h^2(\nabla\nabla f)_a : \mathbf{M}_{2,a} + O(h^3), \tag{16}$$

$$\nabla_a f_a \to \langle\nabla f\rangle_a = \frac{1}{h}\mathbf{M}'_{0,a}(f)_a + (\nabla f)_a \cdot \mathbf{M}'_{1,a} + \frac{1}{2}h(\nabla\nabla f)_a : \mathbf{M}'_{2,a} + \frac{1}{6}h^2(\nabla\nabla\nabla f)_a : \cdot\mathbf{M}'_{3,a} + O(h^3), \tag{17}$$

respectively, where quantities between parentheses denote exact values of the function and its derivatives at the position of particle a and the particle representation of the consistency integrals is given by

$$M_{0,a} = \sum_{b=1}^{n} W_{ab}\Delta V_b, \tag{18}$$

$$\mathbf{M}_{l,a} = \sum_{b=1}^{n} \mathbf{r}_{ba}^{l} W_{ab}\Delta V_b, \quad \text{for} \quad l = 1, 2, \tag{19}$$

$$\mathbf{M}'_{0,a} = \sum_{b=1}^{n} \nabla_a W_{ab}\Delta V_b, \tag{20}$$

$$\mathbf{M}'_{l,a} = \sum_{b=1}^{n} \mathbf{r}_{ba}^{l} \nabla_a W_{ab}\Delta V_b, \quad \text{for} \quad l = 1, 2, 3, \tag{21}$$

where $\mathbf{r}_{ba} = \mathbf{r}_b - \mathbf{r}_a$ and $\Delta V_b = m_b/\rho_b$, with m_b and ρ_b denoting the mass and density of particle b, respectively. According to Eqs. (16) and (17), C^0 particle consistency for the function and its gradient will demand that $M_{0,a} = 1$, $\mathbf{M}'_{0,a} = \mathbf{0}$, and $\mathbf{M}'_{1,a} = \mathbf{I}$ at the position of particle a, while C^1 particle consistency is restored if in addition $\mathbf{M}_{1,a} = \mathbf{0}$ and $\mathbf{M}'_{2,a} = \mathbf{0}^{(3)}$ are satisfied. In particular, restoring C^0 particle consistency implies that the homogeneity and isotropy of the discrete space is preserved, which has as a consequence the conservation of linear and angular momentum in practical calculations (Vignjevic 2009; Sigalotti et al. 2016). The goal here is to track the quality of the particle consistency relations in a true hydrodynamic evolution involving large density and pressure gradients as well as large spatial and temporal variations of the smoothing length. This will allow us to evaluate the degree of consistency that can be achieved when the number of neighbors within the kernel support and the smoothing length are allowed to vary with N according to the scalings $n \sim N^{1/2}$ and $h \sim N^{-1/6}$, which approach asymptotically the joint limit $N \to \infty$, $h \to 0$, and $n \to \infty$ for particle consistency as N is increased.

3. SPH SOLVER

A modified version of the simulation code GADGET-2 is used for the calculations of this paper. The code relies on a fully conservative formulation where the discrete Euler equations are derived via a variational principle from the

discretized Lagrangian of the fluid system (Springel & Hernquist 2002; Springel 2005). As in most SPH formulations, the density estimate is calculated by the summation interpolant

$$\rho_a = \sum_{b=1}^{n} m_b W_{ab}, \tag{22}$$

while the Euler-Lagrange equations of motion for the particles are given by

$$\left(\frac{d\mathbf{v}_a}{dt}\right)_{SPH} = -\sum_{b=1}^{n} m_b \left[\frac{f_a p_a}{\rho_a^2}\nabla_a W_{ab}(h_a) + \frac{f_b p_b}{\rho_b^2}\nabla_b W_{ab}(h_b)\right], \tag{23}$$

where $\mathbf{v}_a$ and p_a are the particle velocity and pressure, respectively, and the factor f_a is defined by

$$f_a = \left(1 + \frac{h_a}{3\rho_a}\frac{\partial \rho_a}{\partial h_a}\right)^{-1}. \tag{24}$$

The velocity of particle a is then updated according to

$$\frac{d\mathbf{v}_a}{dt} = \left(\frac{d\mathbf{v}_a}{dt}\right)_{SPH} + \left(\frac{d\mathbf{v}_a}{dt}\right)_{GRAV} + \left(\frac{d\mathbf{v}_a}{dt}\right)_{AV}, \tag{25}$$

where the last two terms on the right-hand side account for the self-gravitational acceleration and the artificial viscous forces, respectively. The gravitational forces are calculated using a hierarchical multipole expansion, which can be applied in the form of a TreePM method, where short-range forces are calculated with the tree method and long-range forces are determined using mesh-based Fourier methods. A detailed account of the code is given by Springel (2005). Here we shall only briefly describe the improvements that have been incorporated in our version of the code.

One straightforward way of restoring particle consistency and therefore reducing the zeroth-order error terms carried by the SPH representation of the continuity and momentum equations (Read et al. 2010) is just to increase the number of particles within the kernel support. However, conventional kernels, like the widely used cubic B-spline kernel of Monaghan & Lattanzio (1985), suffer from a pairing instability when working with large numbers of neighbors, where particles come into close pairs and become less sensitive to small perturbations within the kernel support (Dehnen & Aly 2012; Price 2012; Hayward et al. 2014). To overcome this difficulty, we have adopted a Wendland C^4 kernel function (Wendland 1995; Dehnen & Aly 2012)

$$W(q,h) = \frac{495}{32\pi h^3}(1-q)^6\left(1 + 6q + \frac{35}{3}q^2\right), \tag{26}$$

if $q \leq 1$ and 0 otherwise, where $q = |\mathbf{r} - \mathbf{r}'|/h$. As was demonstrated by Dehnen & Aly (2012), Wendland functions have positive Fourier transforms and so they can support arbitrarily large numbers of neighbors without favoring a close pairing of particles. Moreover, the exact particle distribution depends on the dynamics of the flow and on the kernel function that is employed. This makes the accuracy assessment of SPH a non-trivial problem. However, Wendland functions are very reluctant to allow for particle motion on a sub-resolution scale and, in contrast to most commonly used kernels, they maintain a very regular particle distribution, even in highly dynamical tests (Rosswog 2015).

A further improvement includes the update of the artificial viscosity switch using the method proposed by Hu et al. (2014). In this method the artificial viscosity term entering on the right-hand side of Eq. (25) is implemented as in GADGET-2 by the common form (Monaghan 1997)

$$\left(\frac{d\mathbf{v}_a}{dt}\right)_{AV} = -\sum_{b=1}^{n} m_b \Pi_{ab}\nabla_a \bar{W}_{ab}, \tag{27}$$

where $\bar{W}_{ab} = [W_{ab}(h_a) + W_{ab}(h_b)]/2$ and

$$\Pi_{ab} = -\frac{1}{2}\frac{\bar{\alpha}_{ab} v_{\rm sig}}{\bar{\rho}_{ab}}\omega_{ab} \quad \text{if} \quad \omega_{ab} < 0, \tag{28}$$

and zero otherwise. Here $\omega_{ab} = (\mathbf{v}_a - \mathbf{v}_b)\cdot\mathbf{r}_{ab}/|\mathbf{r}_{ab}|$, $v_{\rm sig} = c_a + c_b - 3\omega_{ab}$ is the signal speed, c_a is the particle sound speed, $\bar{\rho}_{ab} = (\rho_a + \rho_b)/2$, and $\bar{\alpha}_{ab} = (\alpha_a + \alpha_b)/2$. We note that in the original GADGET-2 code formulation $\alpha_a = \alpha_b = const$. It is well-known that this form of the artificial viscosity introduces excessive dissipation in shear flows, leading to spurious angular momentum transport in the presence of vorticity. Therefore, it is desirable to suppress this excessive dissipation in regions where the vorticity dominates over the velocity divergence (Nelson et al. 2009).

In particular, Morris & Monaghan (1997) proposed individual viscosity coefficients that adapt their values according to velocity-based source terms. Later on, Cullen & Dehnen (2010) improved on this formulation by devising a novel shock indicator based on the total time derivative of the velocity divergence, which distinguishes shocks from purely convergent flows and discriminates between pre- and post-shocked regions. While this prevents false triggering of the artificial viscosity, their method includes a limiter which puts a stronger weight on the velocity divergence than on the vorticity. The artificial viscosity switch proposed by Hu et al. (2014) follows the same principles of that presented by Cullen & Dehnen (2010), except that it now uses a limiter that applies the same weight to the velocity divergence and vorticity. The method consists of calculating the viscosity coefficient through the following steps. A target value of the viscosity coefficient is first calculated using the relation

$$\alpha_{\mathrm{tar},a} = \alpha_{\max} \frac{h_a^2 S_a}{h_a^2 S_a + c_a^2}, \tag{29}$$

where $\alpha_{\max} = 0.75$ and $S_a = \max(0, -\dot{\nabla} \cdot \mathbf{v}_a)$ is the shock indicator. The total time derivative of the velocity divergence is given by $-\dot{\nabla} \cdot \mathbf{v} = d^2 \ln\rho/dt^2$ after differentiation of the continuity equation and the divergence of the velocity is evaluated using the higher-order estimator proposed by Cullen & Dehnen (2010). Hence $\dot{\nabla} \cdot \mathbf{v} < 0$ is indicative of nonlinear flow steepening as occur in pre-shocked regions, while in post-shocked regions $\dot{\nabla} \cdot \mathbf{v} > 0$. The true viscosity coefficient that enters in Eq. (28) is then defined by

$$\alpha_a = \begin{cases} \xi_a \alpha_{\mathrm{tar},a} & \text{if} \quad \alpha_a \le \alpha_{\mathrm{tar},a}, \\ \xi_a \left[\alpha_{\mathrm{tar},a} + (\alpha_a - \alpha_{\mathrm{tar},a}) \exp\left(-\frac{\Delta t}{\tau_a} \right) \right] & \text{if} \quad \alpha_a > \alpha_{\mathrm{tar},a}, \end{cases} \tag{30}$$

where ξ_a is a modified limiter given by

$$\xi_a = \frac{|(\nabla \cdot \mathbf{v})_a|^2}{|(\nabla \cdot \mathbf{v})_a|^2 + |(\nabla \times \mathbf{v})_a|^2 + 0.0001(c_a/h_a)^2}, \tag{31}$$

Δt is the time step, and $\tau_a = 10h_a/v_{\mathrm{sig}}$ is the decay time with a decay speed equal to

$$v_{\mathrm{decay}} = \max_{|\mathbf{r}_{ab}| \le h_a} [\bar{c}_{ab} - \min(0, \omega_{ab})], \tag{32}$$

where $\bar{c}_{ab} = (c_a + c_b)/2$. This method, which is referred to as an artificial viscosity with a strong limiter, suppresses viscous dissipation in subsonically convergent flows and ensures that α_a rises rapidly up to $\alpha_{\max}$ when the converging flow becomes supersonic. This is a desirable property in protostellar collapse simulations where holding α_a to a fixed constant value during the evolution may cause unphysical dissipation of local velocity differences away from shocks. Such adverse effects of the artificial viscosity are responsible for the oversmoothing of weak shocks as well as the damping of adiabatic oscillations and shear flows, thereby seriously affecting the outcome of the simulations.

4. TEST PROBLEMS

4.1. *Particle consistency relations for a set of points*

We first test the quality of the first few moments in relations (18)-(21) for a static set of $N = 64^3$ points distributed within a cube of length $L = 1$, density $\rho = 1$, pressure $p = 1$, and sound speed $c^2 = \gamma p/\rho$, with $\gamma = 5/3$. Two different particle distributions are considered: a glass-like configuration and a random distribution. A similar test problem was employed by Zhu et al. (2015) to determine the quality of the discrete normalization condition given by relation (18) as the number of neighbors is increased from $n = 48$ to 3200. Here the glass distribution was obtained from GADGET-2 by enabling the corresponding code option and starting with **a random distribution** of SPH particles and an expansion factor $a = 0.01$ (Couchman et al. 1995; White 1996). The resulting outcome is then evolved hydrodynamically up to a time $t = 1.1$ in code units, using an isothermal equation of state, periodic boundary conditions at the edges of the box, and excluding self-gravity. As the system evolves toward a relaxed state, the distributions of quantities, such as the smoothing length, the density, and the discrete moments given by relations (18)-(21) tend to normal distributions. The evolution ends up with an equilibrium configuration in which all particles have approximately equal SPH densities (≈ 1).

In real SPH applications, the distances between neighboring particle pairs tend to equilibrate due to pressure forces, which makes the interpolation errors much smaller and the irregularity of the particle distribution more ordered than for a random distribution, where particles sample the fluid in a Poissonian fashion. In this sense, a random configuration represents an extreme case for SPH

simulations. In contrast, a glass configuration mimics the other extreme case where the particle distribution is quasi-regular and almost force-free. Although a random distribution rarely occurs in SPH, except perhaps in highly turbulent flows where particles are highly disordered and SPH is unable to re-order the particles, we analyze the quality of the density estimate and discrete moments of the kernel (and kernel gradient) for a random distribution with the only purpose of comparing with the results obtained by Zhu et al. (2015).

The top and bottom panels of Figure 1 show histograms of the particle density estimate [Eq. (22)] with increasing n from 48 to 3200 as in Zhu et al. (2015) for the glass and random particle distributions, respectively. As expected, the density distribution for the glass configuration is much narrower than for the randomly distributed points. In the former case, as n is increased the density distribution approaches a Dirac-δ distribution, while in the latter case, the distribution slowly approaches a Gaussian shape with a peak at $\rho = 1$. Also, for small values of n the density distribution shows long tails for the random configuration which are not present for the glass distribution, at least when $n \geq 120$. Zhu et al. (2015) argued that such long tails are due to an overestimate of the density produced by the particle self-contribution in Eq. (22) when the SPH particles are randomly spaced. **While this result is well-known, it can also be derived analytically from Eq. (22) given the mass of the particles, their number and actual distribution within the kernel volume, and the form of the kernel function. However, using the $\mathbf{M}_4$ kernel of Monaghan & Lattanzio (1985), Whitworth et al. (1995) demonstrated that the overestimate in density occurs because a random distribution produces a fluctuating density field, where the particle positions are correlated with the overdense fluctuations and anticorrelated with the underdense fluctuations. In other words, the expectation value of the density at the location of a particle will be overestimated by a value almost exactly equal to the "self-density". This is the reason why it seems appropriate to exclude the particle self-contribution from Eq. (22). Whitworth et al. (1995) concluded that as soon as the particle positions are settled before they are allowed to evolve dynamically, exclusion of the self-contribution will lead to a significant error because the particle distribution will cease to be random and the density fluctuations will be removed**. Table 1 lists the standard deviation, $\sigma(\rho)$, and expectation value, $\langle\rho\rangle_e$, of the density measured from the distributions of Figure 1. For both particle configurations, $\sigma(\rho)$ decreases with increasing n, while the value of $\langle\rho\rangle_e$ becomes close to unity when $n \gtrsim 480$ for a glass configuration and $n \gtrsim 1600$ for a random distribution. This agrees with the $\sim n^{-1/2}$ and n^{-1} trends of $\sigma(\rho)$ as a function of n found by Zhu et al. (2015) for a truly random and a glass-like configuration, respectively. Since the results of Figure 1 are consistent with the findings of Zhu et al. (2015) for these tests, we feel confident to proceed with a similar statistical analysis to measure the quality of the discrete moments as n is increased.

According to the series expansions (16) and (17), the error in the density and density gradient estimates separates into two contributions: one due to the local value of h and the other due to the discrete values of the moments. Since the latter are independent of h, they will only depend on the number of neighbors within the kernel support. This observation introduces a subtle difference between the meaning of consistency and accuracy in SPH. Consistency demands that $n \to \infty$, while accuracy demands that $n \to \infty$ and $h \to 0$ in order to have convergent results in the limit $N \to \infty$. Therefore, we can achieve approximate particle consistency and improved accuracy as n is increased and h is decreased with N.

To achieve C^0 consistency, the parameter $M_{0,a}$ and the mean of the elements of matrix $\mathbf{M}'_{1,a}$ should peak around 1, while the mean of the components of vector $\mathbf{M}'_{0,a}$ should follow a peaked distribution around 0. Moreover, C^1 consistency will additionally require that the mean of the components of $\mathbf{M}_{1,a}$ and the mean of the elements of matrix $\mathbf{M}'_{2,a}$ both peak around 0. The distributions of all these quantities are plotted in Figures 2 and 3 for the glass and random configurations, respectively. We may see that for the glass configuration the distributions follow the desired behavior and approach a Dirac-δ function as n is increased, indicating that approximate C^1 consistency is achieved for the density and its gradient when $n = 3200$. Conversely, for a random configuration the distributions approach Gaussian-like shapes with peaks close to the continuum values. For both particle configurations the distributions of $M_{0,a}$ peak at values lower than 1 for small n, suggesting an overestimation of the particle density for small numbers of neighbors. Table 1 lists the standard deviations and expectation values of these moments as calculated by fitting a Gaussian function to the histograms of Figures 2 and 3. From these values we see that very good C^0 and C^1 consistencies are achieved for the glass configuration. A stronger sensitivity to the particle distribution is observed for $\mathbf{M}'_{0,a}$, which is exacerbated for the random configuration. In this case, the standard deviation of the distribution is consistently larger for smaller n and converges to zero rather slowly compared to the glass configuration. Evidently, $\mathbf{M}'_{0,a}$ seems to be more sensitive to the degree of particle disorder than the other parameters for this test, implying a higher error in the SPH representation of the gradient. Although this error depends on the quality of the particle

distribution, it can be regulated by further increasing the number of neighbors since the standard deviation is expected to follow a trend between $n^{-1/2}$ and n^{-1} in actual SPH calculations. Also, note that the expectation values of $\mathbf{M}_{1,a}$, $\mathbf{M}'_{0,a}$, and $\mathbf{M}'_{2,a}$ are always zero because of the symmetry of the kernel.

The required computational cost in CPU time for a complete run is nearly the same for the standard and modified GADGET-2 code. However, the computational cost increases almost linearly with n for fixed N. For instance, a run with $n = 3200$ took about 11 s compared to ~ 0.34 s for $n = 64$, implying a factor of ~ 32 more CPU time. Thus, increasing the number of neighbors increases the computational cost, which is the price that has to be paid when SPH is used as a numerically consistent method. Also, Zhu et al. (2015) argued that when n is made to vary with N as $N^{0.5}$, the computational cost scales with N as $O(N^{1.5})$ rather than as $O(N)$ as for traditional choices of n.

4.2. *Two-dimensional Keplerian ring*

We now test the performance of our implemented artificial viscosity for an equilibrium ring of isothermal gas rotating about a central point mass. This test is the same documented by Cullen & Dehnen (2010) and Hu et al. (2014). Self-gravity of the ring is neglected and perfect balance between pressure forces, gravitational attraction from the central point mass, and centrifugal forces is assumed. The surface density of the gas is given by the Gaussian profile

$$\Sigma(r) = \frac{1}{m} \exp\left[\frac{-(r - r_0)^2}{2\sigma^2}\right], \tag{33}$$

where m is the mass of the ring, r is the radial distance from the central point mass ($r = 0$), $r_0 = 10$, and $\sigma = 1.25$ is the width of the ring. For the central point mass we set $GM = 1000$, where G is the gravitational constant and $M \gg m$. The ring is filled with $N = 9987$ particles, initially distributed using the method of Cartwright et al. (2009). With these parameters, the ring is in differential rotation with an azimuthal velocity $v_\phi = \sqrt{GM/r} = 10$ and a rotation period $T = 2\pi$ at $r = r_0$. The sound speed is set to $c = 0.01$. This value is much smaller than the azimuthal velocity so that dynamical instabilities in the ring are expected to occur only after many rotation periods (Cullen & Dehnen 2010). Under Keplerian differential rotation the flow is shearing and therefore any viscosity may cause the ring to break up (Lynden-Bell & Pringle 1974), with the instability initiating at its inner edge (Maddison et al. 1996).

Figure 4 shows the ring configuration as obtained using four different SPH schemes. The times are given in code units. When GADGET-2 is used with the cubic B-spline kernel and $n = 12$ neighbors together with the standard artificial viscosity formulation with a constant coefficient $\alpha = 0.8$ (Fig. 4a), the ring becomes unstable at $t \approx 3.8$ (corresponding to $\approx 0.6T$). At $t = 12$, i.e., after approximately two rotation periods, the inner edge instability is well-developed and the ring is close to break up. When the same run is repeated using Hu et al. (2014) scheme for the artificial viscosity with the higher-order velocity divergence estimator proposed by Cullen & Dehnen (2010) and α varying in the interval $[0, 0.8]$, the instability manifests in the form of particle clusterings and voids in the particle distribution, resembling a sort of sticking instability, as shown in Figure 4b at $t = 49$ (corresponding to ≈ 7.8 rotation periods). The calculation stops soon thereafter because of failure of the TreePM algorithm when clustered particles become too close to one another. Only little improvement is obtained when using the standard artificial viscosity formulation and the Wendland C^4 function with $n = 120$ neighbors as the ring becomes unstable after about one rotation period ($t \approx 6.6$). Figure 4c shows progress of the instability at a later time ($t = 15$). Therefore, changing the cubic B-spline kernel with a Wendland C^4 function with $n = 120$, or even larger n, while maintaining the standard artificial viscosity causes the instability to grow a little more slowly. Only when this latter run is repeated using Hu et al. (2014) scheme for the artificial viscosity does the ring stay stable for more than 20 rotation periods (Fig. 4d). The ring preserves its particle configuration and remains stable even when the evolution is followed for more than 30 rotation periods.

5. PROTOSTELLAR COLLAPSE SIMULATIONS

We now test the consistency and accuracy of our implemented SPH method for numerical hydrodynamical calculations involving large density and pressure gradients as well as variable smoothing lengths. As a problem we choose the collapse and fragmentation of an isolated molecular cloud core. The templates for the model clouds correspond to the well-known standard isothermal test case in the variant calculated by Burkert & Bodenheimer (1993) and the centrally condensed, Gaussian cloud advanced by Boss (1991).

5.1. *Initial conditions*

5.1.1. *Standard isothermal cloud*

The standard isothermal test case starts from a uniform density ($\rho_0 = 3.82\times10^{-18}$ g cm^{-3}) sphere of mass $M = 1M_\odot$, radius $R = 4.99 \times 10^{16}$ cm, temperature $T = 10$ K, and solid-body rotation $\omega = 7.2 \times 10^{-13}$ s^{-1}. The model has ideal gas thermodynamics with a mean molecular weight $\mu \approx 3$ and an isothermal sound speed $c_{\rm iso} \approx 1.66 \times 10^4$ cm s^{-1}. With these parameters the initial mean free-fall time is $t_{\rm ff} \approx 1.07 \times 10^{12}$ s. In order to favor fragmentation into a binary system, the uniform density background is perturbed azimuthally as

$$\rho = \rho_0 \left[1 + 0.1 \cos(2\phi)\right], \tag{34}$$

where ϕ is the angle about the spinning z-axis. With these parameters the ratios of thermal and rotational energies to the absolute value of the gravitational energy are $\alpha \approx 0.26$ and $\beta \approx 0.16$, respectively.

5.1.2. *Gaussian cloud*

The Gaussian cloud corresponds to a centrally condensed sphere of the same mass and radius as the standard isothermal cloud. The radial central condensation is given by

$$\rho(r) = \rho_{\rm c} \exp\left[-\left(\frac{r}{b}\right)^2\right], \tag{35}$$

where $\rho_{\rm c} = 1.7 \times 10^{-17}$ g cm^{-3} is the initial central density and $b \approx 0.578R$. This produces a central density 20 times higher than the density at the outer edge. Solid-body rotation is assumed at the rate $\omega = 1.0 \times 10^{-12}$ s^{-1}. The gas has a temperature of 10 K, a chemical composition corresponding to a mean molecular weight $\mu \approx 2.28$, and an isothermal sound speed $c_{\rm iso} \approx 1.90 \times 10^4$ cm s^{-1}. The central free-fall time is $t_{\rm ff} \approx 5.10 \times 10^{11}$ s and the radial density distribution is azimuthally perturbed using Eq. (34). With this choice of the parameters, the values of α and β are the same as for the uniform-density, standard isothermal test.

5.1.3. *Equation of state*

A barotropic pressure-density relation of the form (Boss et al. 2000)

$$p = c_{\rm iso}^2 \rho + K\rho^\gamma, \tag{36}$$

is used for both the uniform- and Gaussian-cloud models, where $\gamma = 5/3$ and K is a constant determined from equalizing the isothermal and adiabatic parts of Eq. (36) at a critical density $\rho_{\rm crit} = 5.0 \times 10^{-12}$ g cm^{-3} for the isothermal test case and 5.0×10^{-14} g cm^{-3} for the Gaussian cloud, which separates the isothermal from the nonisothermal collapse. The local sound speed is therefore given by

$$c^2 = c_{\rm iso}^2 \left[1 + \left(\frac{\rho}{\rho_{\rm crit}}\right)^{\gamma-1}\right], \tag{37}$$

so that $c \approx c_{\rm iso}$ when $\rho \ll \rho_{\rm crit}$ and $c \approx \gamma^{1/2} c_{\rm iso}$ when $\rho \gg \rho_{\rm crit}$. With these choices of the critical density we allow the standard isothermal cloud to evolve deep into the isothermal collapse to provide direct comparison with previous barotropic SPH calculations by Kitsionas & Whitworth (2002) and Arreaga-García et al. (2007), while a value of $\rho_{\rm crit} = 5.0\times10^{-14}$ g cm^{-3} produces a behavior that is more representative of the near-isothermal phase and fits better the Eddington approximation solution of Boss et al. (2000).

5.1.4. *Initial particle distribution and smoothing length*

All collapse calculations start from a set of points in a glass configuration, which was generated from **randomly distributed particles** using the GADGET-2 glass-making mode. As shown in Table 2, we consider two separate sequences of calculations with varying total number of particles (N) for both the uniform and Gaussian cloud models. Models labeled U1C-U4C correspond to uniform clouds calculated with the standard GADGET-2 using a fixed number of neighbors ($n = 64$), while models U1W-U4W were calculated using our modified GADGET-2 code using a Wendland C^4 function with varying number of neighbors. Similarly, models G1C-G6C and G1W-G6W correspond to Gaussian clouds using the standard (with $n = 64$) and modified code (with varied n), respectively.

For these tests, we use the parameterization provided by Zhu et al. (2015), where h is allowed to vary with N as $h \propto N^{-1/6}$. With this choice we obtain the scaling relations $n \approx 7.61N^{0.503}$ and $h \approx 7.23n^{-0.33}$ so that h decreases as the number of neighbors increases. Thus, choosing the proportionality factor of the scaling $h \propto N^{-1/6}$ as exactly unity gives an exponent for the dependence of h on n that is close to the suggested value of $-1/3$. The variation of h with n is depicted in Figure 5. For small values of n the smoothing length decreases rapidly as n increases and then more slowly at larger values of n, asymptotically approaching zero as $n \to \infty$ as required to restore particle consistency.

We note that models U1W–U4W do not satisfy the Jeans condition for densities above $\approx 5.0 \times 10^{-14}$ g cm^{-3} due to their much larger numbers of neighbors compared to models U1C–U4C. In contrast, models G1W–G6W all meet the Jeans resolution requirements for gravitational fragmentation. However, in order to avoid spurious fragmentation the gravity softening length of each particle, ϵ_a, is evolved with time in step with its corresponding smoothing length h_a so that $\epsilon_a \approx h_a$ (Bate & Burkert 1997). In addition, Hubber et al. (2006) showed that SPH reproduces the analytical Jeans criterion and simulates gravitational fragmentation properly, even at very poor resolution. That is, artificial fragmentation is suppressed in regions where the Jeans mass is less than the minimum resolvable mass, $M_{\min} = nm$, provided the standard kernel-softened gravity ($\epsilon \approx h$) is used, where m is the mass of a single SPH particle. This way unresolved Jeans-unstable condensations are stabilized numerically. Thus, Hubber et al. (2006) concluded that failing to satisfy the Jeans condition simply suppresses true fragmentation in SPH calculations, rather than resulting in artificial fragmentation as in finite-difference codes. Similar conclusions were previously met by Whitworth (1998) through an analytical derivation of the Jeans criterion.

5.2. *Collapse of the uniform cloud*

Although a uniform-density profile is an extreme idealization of a real cloud core, it provides a simple model to learn how nonaxisymmetric perturbations grow from a structureless medium. Perhaps the most illustrative example of this is given by the standard isothermal test case, which was originally proposed by Boss & Bodenheimer (1979) and thereafter used as a benchmark for testing numerical codes studying protostellar collapse and fragmentation processes, with the fairly good agreement that the outcome of the first evolution is the formation of a protostellar binary system (Burkert & Bodenheimer 1993; Truelove et al. 1998; Boss et al. 2000; Kitsionas & Whitworth 2002; Springel 2005; Arreaga-García et al. 2007). Previous highly-resolved SPH calculations for this test over ~ 9 orders of magnitude increase in density and using a limited number of neighbors ($n \approx 64$) have predicted the formation of two elongated fragments connected by a filamentary bar when the maximum density in the fragments has passed $\rho_{\rm crit} = 5.0 \times 10^{-12}$ g cm^{-3} (Kitsionas & Whitworth 2002; Arreaga-García et al. 2007). When the gas within the fragments becomes adiabatic and heats up, their cylindrical collapse slows down. This makes the fragments to approach a rather spherical shape, while the connecting bar, which remains isothermal, collapses to a singular filament with no signs of fragmentation. However, comparisons between all these earlier calculations have been performed with varied total numbers of particles N and a constant number of neighbors $n \approx 64$ or so, and therefore they are likely to suffer from a loss of consistency due to persisting zeroth-order discretization errors, whose magnitudes may even grow at a faster rate when approaching the limit $N \to \infty$ and $h \to 0$ (Read et al. 2010).

Figure 6 displays column density images of the cloud midplane during the collapse of model U4C using the original GADGET-2 formulation with $n = 64$ neighbors. We may see that up to $1.2736 t_{\rm ff}$ (peak density of $\sim 10^{8.91}\rho_0$), the morphology of collapse and the fragmentation details are very similar to previously reported SPH results for this model. A singular bar connecting two quasi-spherical fragments is formed and the details of the fanning-out of the bar close to the binary fragments are also reproduced. However, when the calculation is continued farther in time the binary components undergo rapid rotational disruption into smaller fragments (see the last snapshot at $1.302 t_{\rm ff}$ when the peak density is $\sim 10^{9.74}\rho_0$). Meanwhile the gas within the singular bar becomes adiabatic, hindering its cylindrical collapse and fragmenting along its length into similar small objects. Due to their excess kinetic energy acquired during rotational disruption of the former binary components, some of these fragments collide and merge between them and/or with those coming from the bar breakup, followed by a rather chaotic dynamics at later times. At these stages, the outcomes of models U1C–U4C show no sign of convergence at comparable maximum densities. **However, we note that the lack of convergence is not surprising because at this stage the small-scale fragmentation observed derives from the non-linear amplification of particle noise inherent in SPH, which leads to different patterns as the spatial resolution is increased. This noise arises because mutually repulsive pressure forces between particle pairs do not cancel in all directions simultaneously. It affects the accuracy of SPH and leads to slow convergence rates. On the other hand, the use of the standard artifical viscosity with a constant coefficient leads to spurious angular momentum transport in the presence of vorticity, which may cause the rotational disruption of the binary fragments**.

The time evolution of the distribution of the first few moments given by relations (18)–(21) is depicted in Figure 7 for model U4C. Only the late stages of collapse during the process of fragmentation are shown. All plots represent only particles carrying a density greater than $\rho_{\rm crit}$ as identified from the last snapshot generated during the simulation. Starting from a given point in the evolution, **histograms** for the particle density, smoothing length, and moment distributions are constructed. The gray strips in the plots of Figure 7 correspond to the time evolution of the standard deviations calculated with respect to the maximum of the distributions (marked with the solid lines), where most

particles lie. Hence, the width of the strips at any given time gives the width of the corresponding distribution. This procedure allows us to evaluate the quality of the consistency relations in rapidly evolving regions of high density where the smoothing length is also varying rapidly to guarantee adequate spatial resolution. According to expansions (16) and (17), the trends of the M_0, $\langle \mathbf{M}_0' \rangle$, and $\langle \mathbf{M}_1' \rangle$ distributions are indicative of whether C^0 consistency is achieved during the evolution, while the degree of C^1 consistency is measured by the time evolution of the $\langle \mathbf{M}_1 \rangle$ and $\langle \mathbf{M}_2' \rangle$ distributions. The maxima of the distributions of $\langle \mathbf{M}_1 \rangle$ and $\langle \mathbf{M}_2' \rangle$ always peak at zero because of the symmetry of the kernel. Note that the maxima of the $\langle \mathbf{M}_0' \rangle$ distribution also peak at zero, except toward the end of the evolution when they start to oscillate erratically about a mean value close to zero. As the smoothing length decreases sharply, within the growing fragments, the width of $\langle \mathbf{M}_1 \rangle$ and $\langle \mathbf{M}_2' \rangle$ contracts until approaching a Dirac-δ distribution. In contrast, the width of $\langle \mathbf{M}_0' \rangle$ remains approximately constant. On the other hand, the peaks of the distributions of M_0 and $\langle \mathbf{M}_1' \rangle$ are always below unity, meaning that C^0 consistency is not achieved. The deviations from unity of M_0 are even larger than those of $\langle \mathbf{M}_1' \rangle$, implying that the estimate of the function is more sensitive to the particle discretization errors than the estimate of the gradient. Violation of the normalization condition by the particle approximation means that the calculation of model U4C is even **worse** than first-order accurate. Similar temporal variations of the estimates of the moments were also observed for models U1C–U3C at lower resolution. For all these models, the values of M_0 and $\langle \mathbf{M}_1' \rangle$, which were initially closer to unity, degraded gradually in the course of collapse and the time interval represented in Figure 7 corresponds to that of maximum deviation.

Details of the evolution of models U2W and U4W are shown in Figures 8 and 9, respectively, at comparable maximum densities. As shown in Table 2, model U2W is run with $N = 600000$ and $n = 6121$, while model U4W uses $N = 2400000$ and $n = 12289$, where the initial value of h is set by the relation $h \approx 7.23n^{-0.33}$ (see Fig. 5). Except for small residual differences in the evolution of the maximum density at earlier collapse times, models U2W and U4W shows essentially the same morphology. The same is true for models U1W and U3W. It is important to notice that increasing n with resolution implies reducing the particle discretization errors **and improving the mass resolution as** $M_{\rm min} = nm \sim n^{-1}$. In other words, this means that the particle approximation approaches the kernel approximation. Since models U1C–U4C work with smaller smoothing lengths due to their fixed, low value of n compared to models U1W–U4W for the same N, it is not possible to establish a direct quantitative comparison between both sequences. Indeed this will require recalculating models U1W–U4W with huge amounts of neighbors so that both sequences will have the same value of h but different N. However, working with finer values of h, while losing complete consistency, does not imply higher accuracy and convergence. If C^0 and C^1 consistencies are achieved, it follows that the discrete expansions (16) and (17) tend to their continuous counterparts (13) and (14), respectively, implying second-order accuracy for the particle approximation independently of the numerical value of h. This is the essence of particle consistency in SPH.

The early collapse is qualitatively similar to models U1C–U4C. Initially the cloud flattens about the equatorial plane, producing an isothermal disk with strong shocks on both sides of it. The azimuthal structure of the disk consists of two overdense blobs as a result of the $m = 2$ perturbation seed, which then fall toward the cloud center to merge into a bar with maximum density at its endpoints. Due to converging flow into the bar, it soon grows in mass and undergoes a cylindrical collapse upon itself. The result of this process is the formation of a binary connected by a considerably more massive and thicker bar compared to models U1C–U4C. The basic features of the formation of the binary plus connecting bar are very similar in Figures 8 and 9 despite the difference in spatial resolution. In these models the bar is centrally condensed, a feature which is not clear from models U1C–U4C. The bar as a whole is never seen to contract into a singular filament. The nascent binary cores are spinning about an axis of symmetry passing through their points of maximum density. This causes the bar to fan out close to the fragments and develop well-pronounced spiral arms. As the cores accrete low angular momentum from the connecting bar and the spiral arms, the binary separation decreases and the bar eventually dissipates. Because of its higher initial resolution, model U4W fragments into a wider binary ($t = 1.2869t_{\rm ff}$) compared to model U2W ($t = 1.2973t_{\rm ff}$). As a result of the accretion process, well-defined protostellar disks form around the cores. The size of these disks is of order ~ 50 AU. We note that the outcome of model U2W is very similar to that reported by Klein et al. (1999) for the same initial conditions using their AMR finite-difference method. The last snapshot of Figure 8 shows the binary at an orbital separation of ~ 88 AU, when almost 10% of the cloud mass is cointained by the fragments. A similar binary system is produced by models U3W and U4W but with larger orbital separations (~ 146 AU) compared to model U2W at approximately the same maximum density. However, in model U4W the circumstellar disk of one of the binary cores is seen to fragment into a secondary of mass $\sim 0.02 M_\odot$, which then revolves around the primary with mean orbital separations of $\sim$14–20 AU. The last snapshot of Figure 9 shows the final configuration for model U4W, where a new small fragment ($\sim 0.006 M_\odot$) has emerged from the residual bar material, which moves toward the binary core on the right side and so it will

probably merge. The calculation was terminated at this time because of the increasingly small time steps at this stage of the evolution. About 9% of the total cloud mass is contained by the cores in models U3W and U4W. The formation of an apparently stable triple system in the highest resolved calculation shows that the standard isothermal test is a demanding one.

Fragment disruption is never seen to occur and very good convergence is achieved. This is a big difference with models U1C–U4C, where the cores disrupted into smaller fragments and the connecting bar experienced multiple fragmentation along its length into similar small fragments. **The use of a Wendland function with a large number of neighbors provides sufficient sampling of the kernel volumes and reduces particle noise compared to the case of models U1C–U4C. Therefore, fragmentation of the protostellar disk leading to a close binary in model U4W is not the result of noise amplification but rather of the nonlinear growth of a gravitational instability as the mass resolution is improved (see Section 5.4 below)**. The effects of increasing the number of neighbors from $n = 30$ to 200, while keeping N fixed were previously studied by Commerçon et al. (2008) for initially uniform clouds starting with stronger thermal support ($\alpha = 0.50$) and lower rotation ($\beta = 0.04$) than the models considered here. They found that increasing the ratio n/N speeds up fragmentation because increasing n for a fixed N decreases the spatial resolution as h necessarily increases. We note that this strategy is different from the one implemented here where full SPH consistency demands that $n/N \to 0$ and $h \to 0$ in the limit $N \to \infty$ and $n \to \infty$ (Rasio 2000). The impact of varying the initial temperature on the collapse of the standard isothermal test case was recently studied by Riaz et al. (2014) using their GRADSPH code. In particular, when the temperature is set to $T = 10$ K they obtain a stable binary system in a similar way as shown in Figure 8 for model U2W. However, their calculations differ from ours in the value of $\rho_{\rm crit}$. **If $\rho_{\rm crit}$ is two orders of magnitude higher, this surely lengthens the isothermal phase of collapse and favors** the formation of a stable binary system (see, for instance, Arreaga-García et al. (2007) for similar calculations with the standard GADGET-2 code; their Figures 5 and 6). The effects of the magnetic field on a variant of the standard isothermal test case have been investigated by Bürzle et al. (2011) using the development version of GADGET-3 extended to include the magnetic field. Setting $\rho_{\rm crit} = 1.0 \times 10^{-14}$ g cm^{-3}, they also obtained a stable binary system as in Arreaga-García et al. (2007) and Riaz et al. (2014) for a purely hydrodynamical calculation with no magnetic field.

Figures 10 and 11 show the time evolution of the estimates of the moments for models U2W and U4W. Compared to Figure 7, the moments M_0 and $\langle \mathbf{M}_1' \rangle$ are now closer to unity for most of the evolution, implying that approximate C^0 consistency is achieved in this set of calculations, except after $\approx 1.26 t_{\rm ff}$ when the degree of C^0 consistency is temporally lost within the fragment regions (see Fig. 10 for model U2W). This occurs precisely when h changes rapidly to ensure sufficient spatial resolution within the higher-density regions. After this adaptive process, i.e., when the variations of h slow down, C^0 consistency is rapidly restored (after about $1.34 t_{\rm ff}$ for model U2W and $1.31 t_{\rm ff}$ for model U4W). This is not surprising since it is well-known that adaptive SPH calculations severely affect the consistency of the method (Liu & Liu 2006). However, this temporal loss of consistency can be cured by increasing further both n and N such that the ratio $n/N \to 0$. This can be seen by comparing Figures 10 and 11, where the interval of inconsistency is reduced and the quality of the estimates improves for model U4W. If we take the temporal mean of the maximum of the distributions of M_0 and $\langle \mathbf{M}_1' \rangle$ over the full interval, the result is very close to unity, implying that C^0 consistency is maintained on average. This is not the case for models U1C–U4C. The maximum of the distributions for the other moments in Figures 10 and 11 are seen to exhibit erratic oscillations about a mean value close to zero. However, the amplitudes of the oscillations are much smaller for model U4W than for model U2W, implying that approximate C^1 consistency is better achieved by the former model. Therefore, we may conclude that model U4W is actually closer to second-order accuracy **and exhibits less noise than its counterpart models at lower resolution**.

5.3. *Collapse of the Gaussian cloud*

Calculations of the protostellar collapse starting from centrally condensed, Gaussian density variations are of greater interest to understand the process of binary fragmentation. A sequence of models similar to G1C–G6C with increasing spatial resolution and fixed $n(= 64)$ was previously calculated by Arreaga-García et al. (2007) using the standard GADGET-2 code (their models G1B–G6B). As the resolution was progressively increased from $N = 0.6$ to 10 million particles, they obtained apparent convergence to a binary system. In order to separate the effects of the artificial viscosity from those of improved consistency on fragmentation, we have run this set of models using the standard GADGET-2 code with n fixed to 64 neighbors and our improved artificial viscosity method for approximately the same range of resolutions explored by Arreaga-García et al. (2007) (see Table 2). In this case, the sequence of calculations G1C–G6C all produced triple systems, consisting of a bound binary plus an ejected third fragment escaping to infinity for models G1C and G2C. In contrast, models G3C–G6C also produced a bound binary with the third fragment now

orbiting around the binary core at distances from ~ 4 to 5 times larger than the binary separation. Although the outcome is the same for all models, the details of the final patterns and properties of the fragments are not the same implying a lack of convergence which can be associated with a loss of C^0 consistency as revealed by the time evolution of the distributions of the estimates of M_0 and $\langle \mathbf{M}'_1 \rangle$. As was outlined before, the form of the artificial viscosity affects the outcome of the simulations. Unphysical dissipation of local velocity gradients away from shocks in the calculations of Arreaga-García et al. (2007) is likely to be the cause of the differences with the outcomes of sequence G1C–G6C.

We now describe the results of models G1W–G6W, which were run using the modified GADGET-2 code with increasing number of neighbors. The initial phase of collapse for these models is qualitatively similar to that observed for models G1C–G6C. That is, up to the point where $\rho_{\rm max} = \rho_{\rm crit}$, the cloud evolves to a centrally condensed, flat disk. When the disk becomes adiabatic, it expands due to increasing pressure forces and deforms by rotational effects into a central bar. Because of further rotation, the bar **wraps** up and becomes S-shaped. After about a rotation period of the central bar, the S-shaped structure grows in size and develops long arms. Meantime, the bar continues rotating and collapses into a central blob. By this time, the S-shaped structure has already deformed and two satellite fragments form at the end parts of the winding arms and at the same distance from the central core, giving rise to a ternary core. From top to down, Figure 12 shows column density images of the evolution of models G3W–G6W at comparable maximum densities and same times. It is evident from the first and second column of images that fragmentation is anticipated when the resolution is increased. However, from the last column we may see that reasonably good convergence is achieved by the highly resolved calculations at comparable maximum densities and times. By $2.0192 t_{\rm ff}$, the fragments are well-defined and evolving as separate entities from the parent cloud. They contain about 13.2% (G3W), 8.4% (G4W), 8.5% (G5W), and 8.5% (G6W) of the total cloud mass, while the separations of the two satellite fragments from the central core are (~ 298 AU) for G3W, (~ 279 AU) for G4W, (~ 289 AU) for G5W, and (288 AU) for G6W.

Figures 13 and 14 depict the time evolution of the distribution of the estimates of the moments for models G3W and G6W. As for the standard isothermal case, only the late evolution is represented in both figures and the distributions are constructed by considering only particles with densities $> \rho_{\rm crit}$. Approximate C^0 and C^1 consistencies are achieved in both cases. However, by comparing these two figures we may see that the quality of the simulation improves for model G6W working with higher values of n and N. Therefore, as the values of n and N are increased, the particle discretization errors decay asymptotically and the calculations become closer to second-order accuracy. As was stated by Commerçon et al. (2008), in studies of protostellar collapse and fragmentation it is more difficult to attain convergence for low than for high thermal support. The point is that in the case of low thermal support the dynamics of the flow is likely to become highly nonlinear faster than in clouds with high thermal support. The same is also true for models where the isothermal phase of collapse is prolonged by choosing high values of the critical density, as is indeed the case of models U1W–U4W, where $\rho_{\rm crit} = 5.0 \times 10^{-12}$ g cm^{-3}. According to expansions (16) and (17), if C^1 particle consistency is restored, the errors carried by the estimates of a function and its gradient match those for the kernel approximation ($\sim h^2$). However, as n and N are increased, h decreases (see Figure 5). Thus, decreasing the size of the kernel not only improves the resolution but also favors the growth of nonlinearity at smaller scales. If thermal support is retarded, then nonlinear behavior may amplify and lead to further fragmentation. This is precisely the difference between the outcomes of models U1W–U3W (Figure 8) and model U4W (Figure 9), where further fragmentation is observed. This is not the case in Figure 12, where the transition from isothermal to adiabatic collapse is anticipated, and the higher resolution calculations provide almost the same fragmentation time and pattern.

5.4. *Protostellar disk fragmentation*

The mass contained within the kernel volume scales with h as $\sim h^3$. Therefore, if $h \sim n^{-1/3}$ then the minimum mass varies with n as $M_{\rm min} \sim n^{-1}$, implying that large numbers of neighbors leads to improved mass resolution. This aspect makes a big difference with models U1C-U4C and G1C-G6C, which employ a fixed value of $n(=64)$ regardless of the total number of particles. Improving the mass resolution will certainly allow to better resolve small-scale features in the flow during the collapse and fragmentation of protostellar cloud cores. This is the case of the highly resolved models U4W and G4W-G6W, where after large-scale fragmentation, which was seeded here by a background $m = 2$ density variation, well-defined rotating disks were clearly seen to form around the growing fragments as a result of infalling material from the cloud envelope. In particular, Fig. 15 shows enlarged density maps for the evolution of one of the former binary fragments formed in model U4W (see Fig. 9, leftmost fragment at $t = 1.3252 t_{\rm ff}$). As the fragment grows in density, a circumstellar disk forms which then becomes sufficiently massive to develop a two-armed spiral structure associated with the linear

growth stage of a gravitational instability. By this time ($1.3042 t_{\rm ff}$), the mass of the disk is $\approx 0.011\ M_\odot$ compared to $\approx 0.032\ M_\odot$ of the central protostar. The radius of the disk is $R_{\rm disk} \approx 25$ AU and grows to ≈ 36 AU by $t = 1.3109 t_{\rm ff}$ just before fragmentation. According to the Toomre stability criterion, the disk is unstable to axisymmetric perturbations if

$$Q \approx \frac{2M_\star}{M_{\rm disk}} \frac{H}{r} < 1, \tag{38}$$

where $M_\star$ is the mass of the central protostar, H is the disk scale height, and r denotes radial distance from the central protostar. In the above definition we have assumed that the disk is Keplerian and define $H = c/\omega$, where ω is the Keplerian angular velocity at radius r. Taking $r = 20$ AU, which is the approximate radius where fragmentation of the disk occurs, we find that $H/r \approx 0.17$ and the Toomre parameter $Q \approx 0.97$. Soon thereafter, the gravitational instability enters a nonlinear growth phase and the outermost part of one of the arms condenses into a secondary at a distance of ≈ 18 AU from the primary, leading to fragmentation of the disk into a tight binary. The newly formed fragment takes its orbital angular momentum from the rotation of the disk and revolves around the primary in an approximate circular orbit. By $1.327 t_{\rm ff}$, when the calculation is terminated, the primary has a mass of $\approx 0.044\ M_\odot$, while the mass of the secondary is $\approx 0.02\ M_\odot$.

The calculation of model U4W shows that working with 12289 neighbors is enough to resolve small-scale fragmentation due to the gravitational instability of a massive protostellar disk. While this can be seen as a possible mechanism for the formation of binary/multiple stellar systems separated by a few AU, recent observations of the L1448 IRS3B triple system, consisting of two protostars at the center and a third one distant from them, are providing strong support to this conclusion (Tobin et al. 2016). The observations, which were conducted with the Atacama Large Millimeter/submillimeter Array (ALMA), show that the spiral structure in the dusty disk surrounding the young stars is indicative of their having been formed by fragmentation of the disk via a gravitational instability. Hence, differences in distance may be the result of different formation mechanisms. For instance, systems separated by hundreds to thousands AU are likely to be the result of fragmentation of the larger cloud during its early gravitational collapse, while tighter systems with separations of tens of AU may be hierarchical systems formed from disk fragmentation.

Similarly, as shown in Fig. 12, models G1W-G6W collapsed to form a central protostar surrounded by a circumstellar disk, which then experienced fragmentation into two secondaries, forming a tertiary protostellar system. This time the circumstellar disk appears to be larger ($\gtrsim 600$ AU) at the time of fragmentation compared to model U4W because of thermal retardation due to the assumption of a lower value of the critical density ($= 5.0 \times 10^{-14}$ g cm^{-3}) for the Gaussian models. As the ternary fragments grow in density, each of them develop well-pronounced circumstellar disks as shown by the last column of density maps in Fig. 12 for models G4W-G6W.

6. CONCLUSIONS

We have investigated the consistency of smoothed particle hydrodynamics (SPH) in numerical simulation tests of the collapse and fragmentation of rotating molecular cloud cores. A modified version of the simulation code GADGET-2 (Springel 2005) was used for the calculations, where the interpolation kernel was replaced by a Wendland C^4 function to allow support of large numbers of neighbors and an advanced scheme for the artificial viscosity was implemented based on the method proposed by Hu et al. (2014). Approximations to the power-law relations provided by Zhu et al. (2015) were used to set the kernel interpolation parameters, namely the total number of particles N, the smoothing length h, and the number of neighbors n, where h is allowed to vary with N as $h \sim N^{-1/6}$. With this choice, the scalings $h \approx 7.23 n^{-0.33}$ and $n \approx 7.61 N^{0.503}$ were used to set the initial values of h and n for fixed N. As the domain resolution is increased, these scalings comply with the combined limit $N \to \infty$, $h \to 0$, and $n \to \infty$ with $n/N \to 0$ for full SPH consistency (Rasio 2000).

The initial conditions for the protostellar collapse models were chosen to be the "standard isothermal test case" in the variant calculated by Burkert & Bodenheimer (1993) and the centrally condensed, Gaussian cloud advanced by Boss (1991), coupled to a barotropic pressure-density relation to simulate the transition from the isothermal to the nonisothermal collapse. The critical density, separating both regimes, was set to $\rho_{\rm crit} = 5.0 \times 10^{-12}$ g cm^{-3} for the standard isothermal test to provide insight into the role played by n for a case where convergence is more demanding at late stages of the evolution. In contrast, for the Gaussian cloud model $\rho_{\rm crit} = 5.0 \times 10^{-14}$ g cm^{-3}, which

is more representative of the near-isothermal phase (Boss et al. 2000). Since convergence is easier when shortening the isothermal phase of collapse due to thermal retardation, this model has been used to discern the effects of the artificial viscosity on the final outcome by comparing with previous calculations by Arreaga-García et al. (2007).

Two separate sequences of calculations with increasing N were run for both models. One sequence used the standard version of GADGET-2 with fixed $n(= 64)$, while the other sequence was calculated using the modified version of the code with varied n. Over ~ 9 orders of magnitude increase in density, the standard isothermal models with fixed n produced a binary connected by a singular bar in much the same way as reported in previous SPH calculations. However, as the evolution was continued farther in time the binary cores and the bar were seen to fragment into smaller condensations, with the dynamics becoming highly nonlinear and chaotic due to numerical noise amplification. At these stages, even the highly resolved models showed no sign of convergence. In contrast, the models with varied n experienced a similar initial collapse, producing stable binary systems for moderate resolutions ($N \leq 1200000$) and a triple system for $N = 2400000$ due to fragmentation of the disk around one of the binary components into a secondary. **Owing to the higher number of neighbors and hence improved mass resolution for this model, it was possible to resolve the small-scale structure and fragmentation of the disk into a close binary. This mechanism has recently received convincing observational evidence for explaining the formation of close binary/multiple protostellar systems (Tobin et al. 2016)**. On the other hand, the Gaussian clouds using the standard GADGET-2 code with fixed n but with the new scheme of the artificial viscosity produced different outcomes at all resolutions compared to those previously reported by Arreaga-García et al. (2007). In all cases, only qualitative convergence into a triple system was achieved, consisting of a bound binary plus a third core at much higher orbital distances. Evidently, the reduced dissipation and better treatment of shocks implied by the new artificial viscosity had an important impact on the final outcome. With the modified code, all runs also produced a final triple system but with a quite different pattern. In this case, the highly resolved runs were seen to converge at comparable maximum densities and times.

The degree of consistency of the calculations was measured by tracking how well the kernel consistency relations were reproduced by the particle approximation. From the time evolution of the estimates of the moments of the kernel it was clear that all calculations with fixed $n(= 64)$ were inconsistent. The normalization condition of the kernel and the first moment of the gradient always diverged from unity, with the maximum deviations occurring at the late stages of the evolution just after the fragmentation period when the fragments were growing in density and h was varying rapidly to ensure adequate spatial resolution, meaning that C^0 consistency was not achieved by these models. Thus, violation of the normalization condition by the particle approximation implies that these calculations are even **worse** than first-order accurate due to persisting zeroth-order discretization errors (Read et al. 2010). In contrast, approximate C^0 and C^1 consistencies were achieved by all models when n was allowed to vary with N. However, loss of C^0 consistency was temporally observed within the fragment regions due to rapid variations of h there, confirming previous expectations that adaptive kernels severely affect the consistency of SPH (Liu & Liu 2006). After this adaptive process, the variations of h in the high-density regions slowed down and C^0 consistency was rapidly restored by the models. In both sequences of calculations, as n and N are increased the interval and degree of inconsistency are progressively reduced and the quality of the calculations is improved. On the other hand, the temporal means of the estimates of the normalization condition of the kernel and the first moment of the gradient over the full interval, where consistency is lost and then restored, are seen to peak very close to unity, implying that C^0 consistency is achieved on average within the fragment regions. Since the estimates of the second moments are always close to zero, approximate C^1 consistency is also achieved. We may therefore conclude that the simulations presented here are actually close to second-order accuracy.

As a final remark, it has been demonstrated that C^0 particle consistency for both the estimates of a function and its gradient implies preservation of the homogeneity and isotropy of the discrete space, which have as consequences conservation of the linear and angular momentum, respectively (Vignjevic 2009; Sigalotti et al. 2016). Therefore, we may expect that local linear and angular momentum are well conserved in our consistent collapse calculations. However, it would be interesting to quantify numerically the degree of angular momentum conservation when C^0 consistency is achieved in the limit $n/N \to 0$. Due to its Lagrangian character, SPH provides direct access to the initial angular momentum of particles so that any loss can be easily quantified following a similar analysis to that developed by Commerçon et al. (2008). Future studies in this line will deal with the impact of consistency on angular momentum conservation and how to address the Jeans-resolution requirement under large numbers of neighbors.

We thank the anonymous referee for raising a number of comments and suggestions that have im-

proved the style and content of the manuscript. In particular, his/her comment on the relation between consistency and mass resolution is much acknowledged. The calculations of this paper were performed using the computing facilities of ABACUS-Centro de Matemáticas Aplicadas y Cómputo de Alto Rendimiento of Cinvestav-IPN. This work was partially supported by ABACUS through the CONACyT grant EDOMEX-2011-C01-165873 and by the Departamento de Ciencias Básicas e Ingeniería (CBI) of the Universidad Autónoma Metropolitana–Azcapotzalco (UAM-A), the Instituto de Ciencias Básicas e Ingenierías of the Universidad Autónoma del Estado de Hidalgo (UAEH), and the Instituto Venezolano de Investigaciones Científicas (IVIC) through internal funds.

REFERENCES

Arreaga-García, G., Klapp, J., Sigalotti, L. Di G., & Gabbasov, R. 2007, ApJ, 666, 290
Bate, M. R., & Burkert, A. 1997, MNRAS, 288, 1060
Bonet, J., & Lok, T.-S. L. 1999, Comput. Meth. Appl. Mech. Eng., 180, 97
Boss, A. P., & Bodenheimer, P. 1979, ApJ, 234, 289
Boss, A. P. 1991, Nature, 351, 298
Boss, A. P., Fisher, R. T., Klein, R. I., & McKee, C. F. 2000, ApJ, 528, 325
Burkert, A., & Bodenheimer, P. 1993, MNRAS, 264, 798
Bürzle, F., Clark, P. C., Stasyszyn, F., Greif, T., Dolag, K., Klessen, R. S., & Nielaba, P. 2011, MNRAS, 412, 171
Cartwright, A., Stamatellos, D., & Whitworth, A. P. 2009, MNRAS, 395, 2373
Chen, J. K., Beraun, J. E., & Jih, C. J. 1999, Comput. Mech., 24, 273
Commerçon, B., Hennebelle, P., Audit, E., Chabrier, G., & Teyssier, R. 2008, Å, 482, 371
Couchman, H. M. P., Thomas, P. A., & Pearce, F. R. 1995, ApJ, 452, 797
Cullen, L., & Dehnen, W. 2010, MNRAS, 408, 669
Dehnen, W., & Aly, H. 2012, MNRAS, 425, 1068
Gingold, R. A., & Monaghan, J. J. 1977, MNRAS, 181, 375
Hayward, C. C., Torrey, P., Springel, V., Hernquist, L., & Vogelsberger, M. 2014, MNRAS, 442, 1992
Hu, C.-Y., Naab, T., Walch, S., Moster, B. P., & Oser, L. 2014, MNRAS, 443, 1173
Hubber, D. A., Goodwin, S. P., & Whitworth, A. P. 2006, A&A, 450, 881
Kitsionas, S., & Whitworth, A. P. 2002, MNRAS, 330, 129
Klein, R. I., Fisher, R. T., McKee, C. F., & Truelove, J. K. 1999, in Numerical Astrophysics 1998, ed. S. Miyama, K. Tomisaka, & T. Hanawa (Dordrecht: Kluwer), 131
Li, S. F., & Liu, W. K. 1996, Comput. Meth. Appl. Mech. Eng., 139, 159
Litvinov, S., Hu, X. Y., & Adams, N. A. 2015, J. Comput. Phys., 301, 394
Liu, M. B., & Liu, G. R. 2006, Appl. Numer. Math., 56, 19
Liu, M. B., Liu, G. R., & Lam, K. Y. 2003, J. Comput. Appl. Math., 155, 263
Lucy, L. B. 1977, AJ, 82, 1013
Lynden-Bell, D., & Pringle, J. E. 1974, MNRAS, 168, 603
Maddison, S. T., Murray, J. R., & Monaghan, J. J. 1996, PASA, 13, 66
Monaghan, J. J. 1992, ARA&A, 30, 543
Monaghan, J. J., & Lattanzio, J. C. 1985, A&A, 149, 135
Monaghan, J. J. 1997, J. Comput. Phys., 136, 298
Morris, J. P., & Monaghan, J. J. 1997, J. Comput. Phys., 136, 41
Nelson, A. F., Wetzstein, M., & Naab, T. 2009, ApJS, 184, 326
Price, D. J. 2012, J. Comput. Phys., 231, 759
Rasio, F. A. 2000, Prog. Theoret. Phys. Suppl., 138, 609
Read, J. I., Hayfield, T., & Agertz, O. 2010, MNRAS, 405, 1513
Riaz, R., Farooqui, S. Z., & Vanaverbeke, S. 2014, MNRAS, 444, 1189
Rosswog, S. 2015, Living Rev. Comput. Astrophys., 1, 1
Sibilla, S. 2015, Comput. Fluids, 118, 148
Sigalotti, L. Di G., Klapp, J., Rendón, O., Vargas, C. A., & Peña-Polo, F. 2016, Appl. Numer. Math., 108, 242
Springel, V. 2005, MNRAS, 364, 1105
Springel, V., & Hernquist, L. 2002, MNRAS, 333, 649
Tobin, J. J., Kratter, K. M., Persson, M. V., et al. 2016, Nature, 538, 483
Truelove, J. K., Klein, R. I., McKee, C. F., Holliman, J. H., Howell, L. H., & Greenough, J. A. 1998, ApJ, 495, 821
Vignjevic, R., & Campbell, J. 2009, in Predictive Modeling of Dynamic Processes, ed. S. Hiermaier (Dordrecht: Springer), 367
Wendland, H. 1995, Adv. Comput. Math., 4, 389
White, S. D. M. 1996, in Cosmology and Large Scale Structure, ed. R. Schaeffer, J. Silk, M. Spiro, & J. Zinn-Justin (Amsterdam: Elsevier), 349
Whitworth, A. P., Bhattal, A. S., Turner, J. A., & Watkins, S. J. 1995, A&A, 301, 929
Whitworth, A. P. 1998, MNRAS, 296, 442
Zhang, G. M., & Batra, R. C. 2004, Comput. Mech., 34, 137
Zhu, Q., Hernquist, L., & Li, Y. 2015, ApJ, 800:6, 13pp

Table 1. Standard deviation $\sigma(\cdot)$ and expectation value $\langle\cdot\rangle_e$ of the density and moments estimates as a function of n.

(1)	(2)	(3)	(4)	(5)	(6)	(7)	(8)	(9)
Glass								
n	48	64	120	240	480	800	1600	3200
$\sigma(\rho)$	3.44(-2)	1.67(-2)	3.31(-3)	1.31(-3)	8.85(-4)	7.03(-4)	4.85(-4)	3.12(-4)
$\langle\rho\rangle_e$	1.05479	1.02380	1.00421	1.00064	1.00003	0.99994	0.99990	0.99989
$\sigma(M_0)$	1.93(-2)	1.04(-2)	2.46(-3)	7.36(-4)	3.89(-4)	3.51(-4)	2.72(-4)	1.87(-4)
$\langle M_0\rangle_e$	0.570	0.678	0.828	0.914	0.957	0.974	0.987	0.993
$\sigma(\mathbf{M}_1)$	2.15(-4)	1.19(-4)	1.75(-5)	4.46 (-6)	3.21(-6)	3.58(-6)	3.96(-6)	3.76(-6)
$\langle\mathbf{M}_1\rangle_e$	0.0	0.0	0.0	0.0	0.0	0.0	0.0	0.0
$\sigma(\mathbf{M}'_0)$	2.63	1.21	1.76(-1)	3.55(-2)	1.08(-2)	7.97(-3)	5.45(-3)	3.18(-3)
$\langle\mathbf{M}'_0\rangle_e$	0.0	0.0	0.0	0.0	0.0	0.0	0.0	0.0
$\sigma(\mathbf{M}'_1)$	3.47(-2)	2.31(-2)	4.73(-3)	9.18(-4)	2.75(-4)	1.75(-4)	1.17(-4)	8.71(-5)
$\langle\mathbf{M}'_1\rangle_e$	0.86317	0.93636	0.98910	0.99792	0.99967	0.99991	0.99997	0.99999
$\sigma(\mathbf{M}'_2)$	2.14(-4)	1.56(-4)	3.93(-5)	6.63(-6)	2.65(-6)	2.38(-6)	2.31(-6)	2.05(-6)
$\langle\mathbf{M}'_2\rangle_e$	0.0	0.0	0.0	0.0	0.0	0.0	0.0	0.0
Random								
$\sigma(\rho)$	2.97(-1)	2.17(-1)	1.20(-1)	6.66(-2)	3.75(-2)	2.45(-2)	1.37(-2)	7.67(-3)
$\langle\rho\rangle_e$	1.22783	1.14226	1.05358	1.01846	1.00626	1.0027	1.00077	1.00019
$\sigma(M_0)$	1.03(-1)	9.54(-2)	6.73(-2)	4.10(-2)	2.39(-2)	1.59(-2)	9.04(-3)	5.06(-3)
$\langle M_0\rangle_e$	0.541	0.659	0.821	0.912	0.956	0.974	0.987	0.993
$\sigma(\mathbf{M}_1)$	6.55(-4)	6.23(-4)	5.04(-4)	3.74(-4)	2.71(-4)	2.13(-4)	1.53(-4)	1.09(-4)
$\langle\mathbf{M}_1\rangle_e$	0.0	0.0	0.0	0.0	0.0	0.0	0.0	0.0
$\sigma(\mathbf{M}'_0)$	10.30	7.73	3.90	1.78	8.06(-1)	4.49(-1)	2.03(-1)	9.13(-2)
$\langle\mathbf{M}'_0\rangle_e$	0.0	0.0	0.0	0.0	0.0	0.0	0.0	0.0
$\sigma(\mathbf{M}'_1)$	8.47(-2)	6.82(-2)	4.11(-2)	2.43(-2)	1.42(-2)	9.49(-3)	5.39(-3)	3.05(-3)
$\langle\mathbf{M}'_1\rangle_e$	0.695	0.794	0.915	0.969	0.989	0.995	0.998	0.999
$\sigma(\mathbf{M}'_2)$	4.32(-4)	3.89(-4)	2.99(-4)	2.24(-4)	1.64(-4)	1.29(-4)	9.21(-5)	6.61(-5)
$\langle\mathbf{M}'_2\rangle_e$	0.0	0.0	0.0	0.0	0.0	0.0	0.0	0.0

Table 2. Collapse models

Model	Total number of particles (N)	Number of neighbors (n)	Final outcome
Uniform clouds			
U1C............	300,000	64	Binary?
U2C............	600,000	64	Binary?
U3C............	1,200,000	64	Binary?
U4C............	2,400,000	64	Binary?
U1W............	300,000	4321	Binary
U2W............	600,000	6121	Binary
U3W............	1,200,000	8673	Binary
U4W............	2,400,000	12289	Triple
Gaussian clouds			
G1C............	300,000	64	Triple
G2C............	600,000	64	Triple
G3C............	1,200,000	64	Triple
G4C............	2,400,000	64	Triple
G5C............	4,800,000	64	Triple
G6C............	9,600,000	64	Triple
G1W............	300,000	4321	Triple
G2W............	600,000	6121	Triple
G3W............	1,200,000	8673	Triple
G4W............	2,400,000	12289	Triple
G5W............	4,800,000	17412	Triple
G6W............	9,600,000	24673	Triple

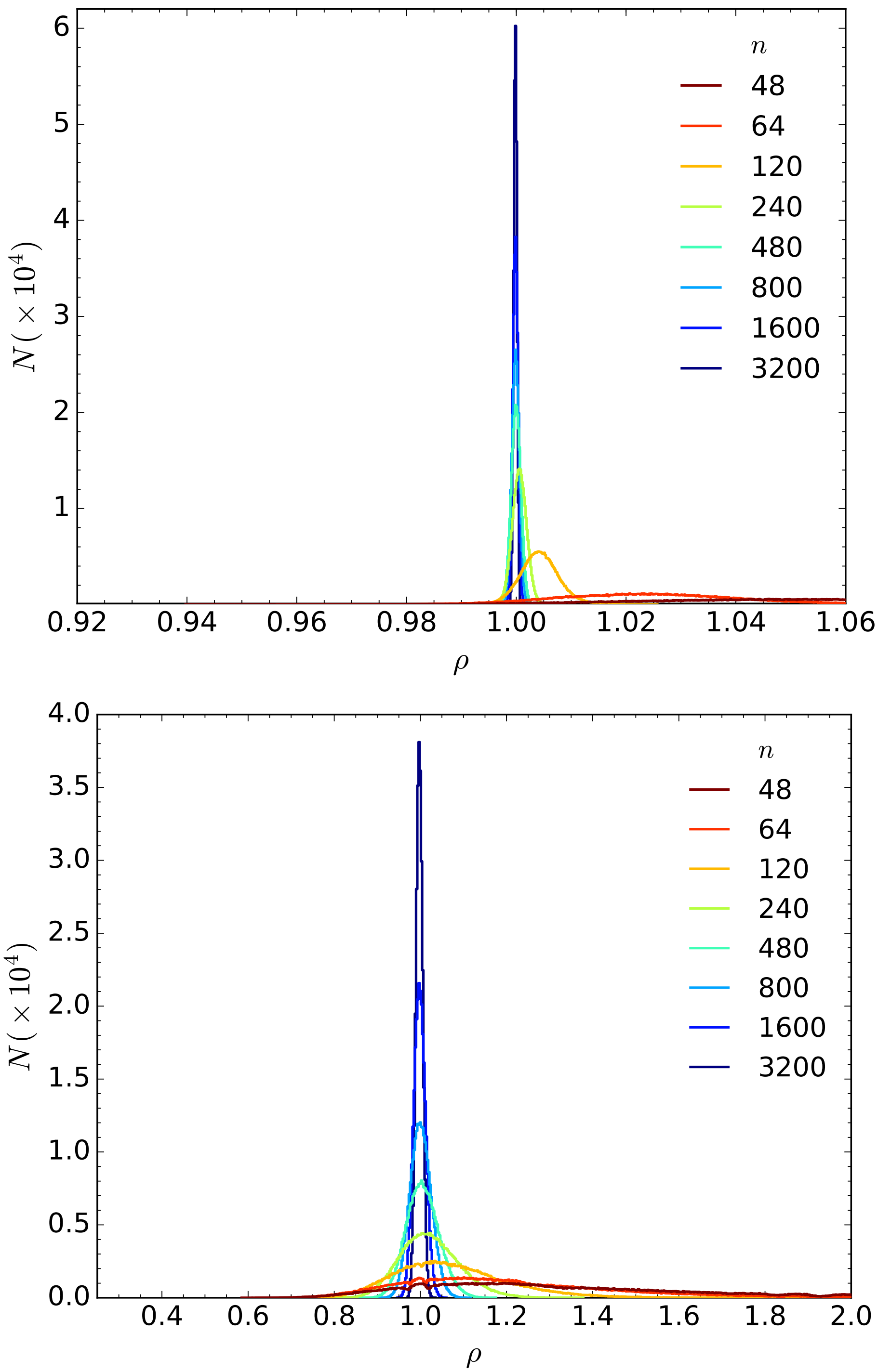

Figure 1. Distribution of the particle density estimates as obtained using the Wendland C^4 function with increasing number of neighbors from $n = 48$ (red curve) to 3200 (dark-blue curve) for a glass (*top*) and a random (*bottom*) particle distribution. In the former case, as n is increased the density distribution approaches a Dirac-δ distribution, while in the latter case, the density distribution looks much broader and approaches a Gaussian-like distribution with a peak at $\rho = 1$ for $n \geq 800$.

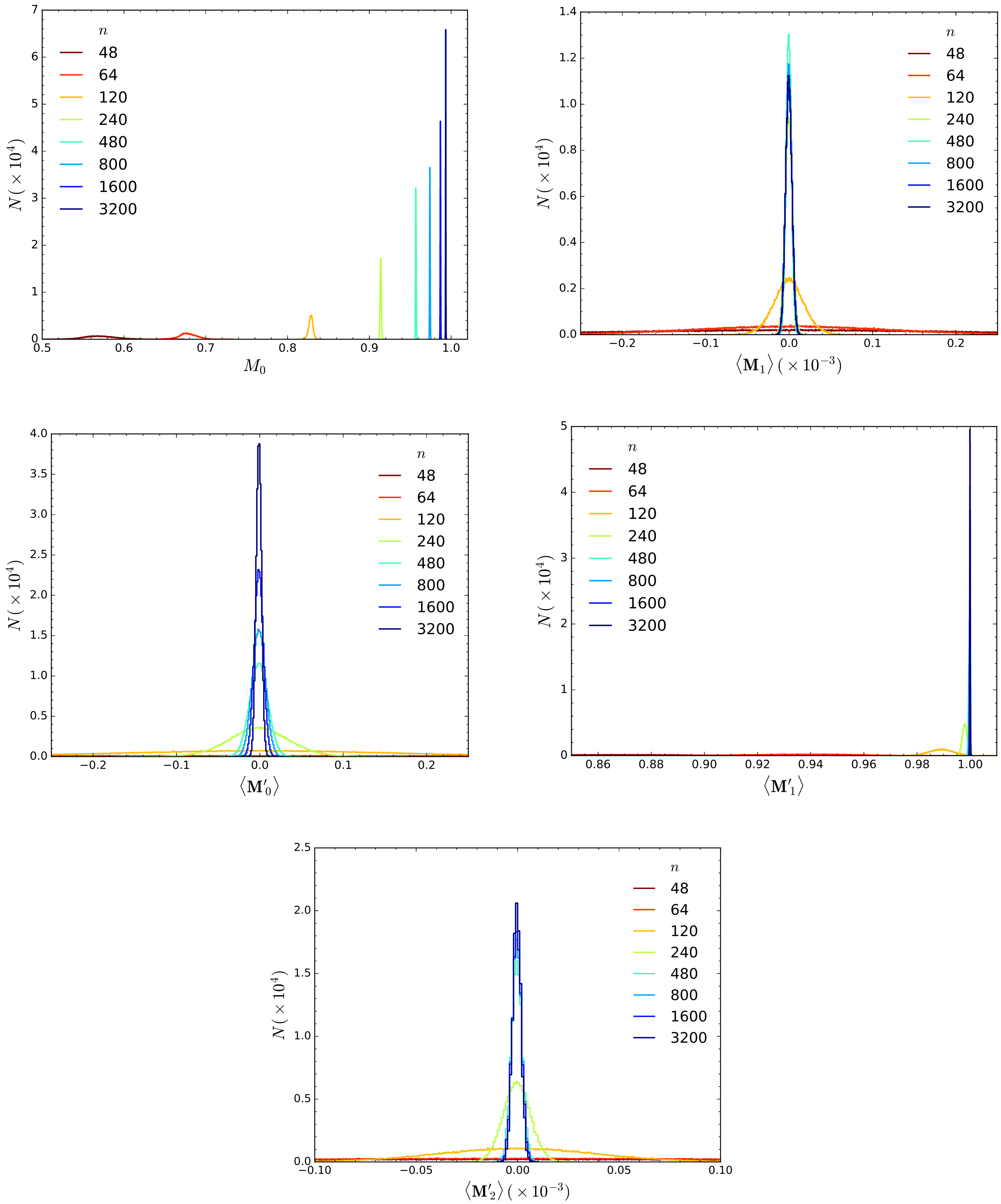

Figure 2. Distributions of the moments of the kernel M_0 and $\mathbf{M}_1$ as given by Eqs. (18) and (19) (*upper plots*) and the moments of the kernel gradient $\mathbf{M}'_0$, $\mathbf{M}'_1$, and $\mathbf{M}'_2$ as given by Eqs. (20) and (21) (*middle and bottom plots*) for the glass particle distribution, using the Wendland C^4 function with increasing number of neighbors from $n = 48$ (red curves) to 3200 (dark-blue curves). $\langle \mathbf{M}_1 \rangle$ and $\langle \mathbf{M}'_0 \rangle$ are the means of the components of $\mathbf{M}_1$ and $\mathbf{M}'_0$, while $\langle \mathbf{M}'_1 \rangle$ and $\langle \mathbf{M}'_2 \rangle$ correspond to the mean of the elements of matrices $\mathbf{M}'_1$ and $\mathbf{M}'_2$, respectively.

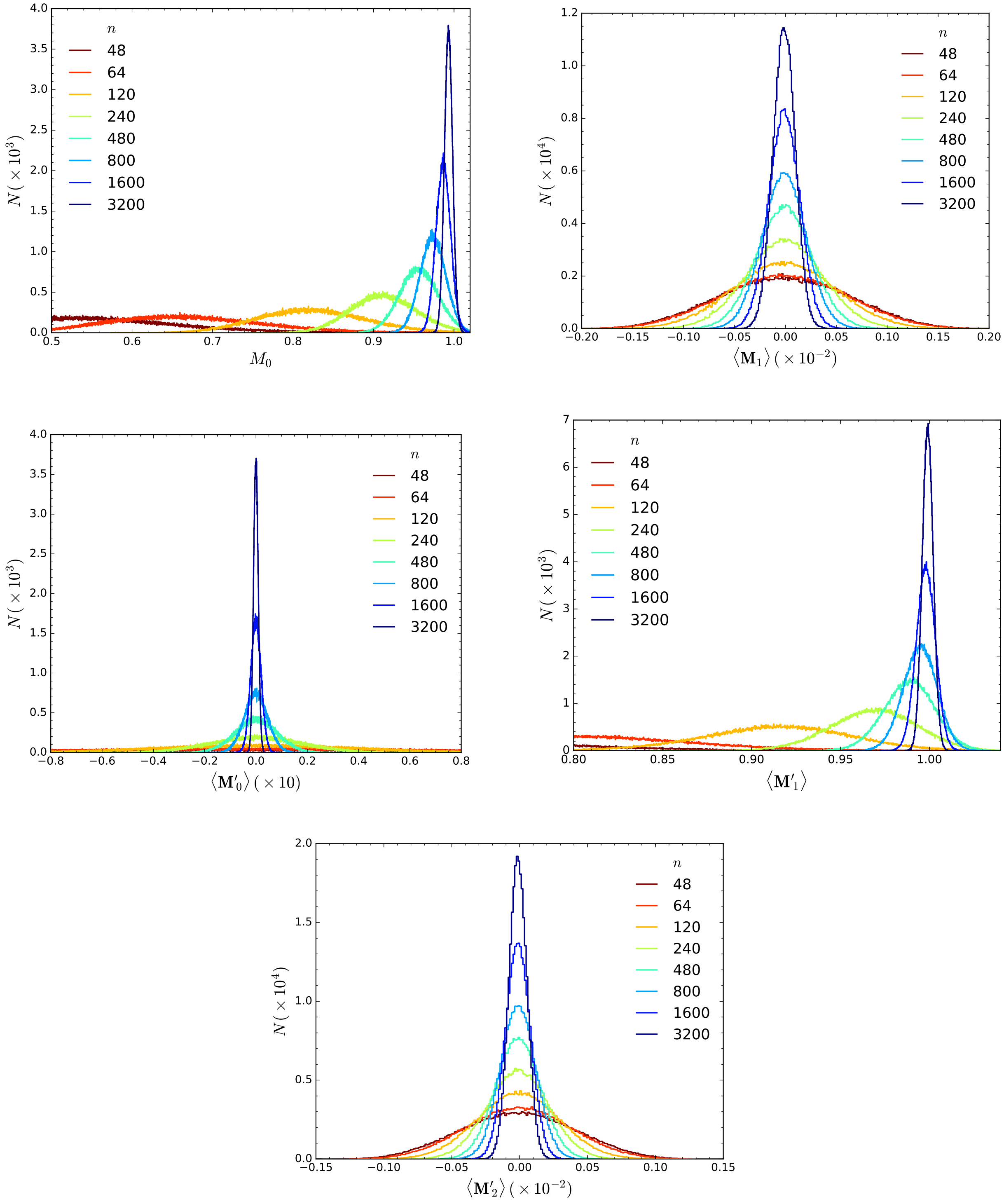

Figure 3. Distributions of the moments of the kernel M_0 and $\mathbf{M}_1$ as given by Eqs. (18) and (19) (*upper plots*) and the moments of the kernel gradient $\mathbf{M}'_0$, $\mathbf{M}'_1$, and $\mathbf{M}'_2$ as given by Eqs. (20) and (21) (*middle and bottom plots*) for the random particle distribution, using the Wendland C^4 function with increasing number of neighbors from $n = 48$ (red curves) to 3200 (dark-blue curves). $\langle \mathbf{M}_1 \rangle$ and $\langle \mathbf{M}'_0 \rangle$ are the means of the components of $\mathbf{M}_1$ and $\mathbf{M}'_0$, while $\langle \mathbf{M}'_1 \rangle$ and $\langle \mathbf{M}'_2 \rangle$ correspond to the mean of the elements of matrices $\mathbf{M}'_1$ and $\mathbf{M}'_2$, respectively.

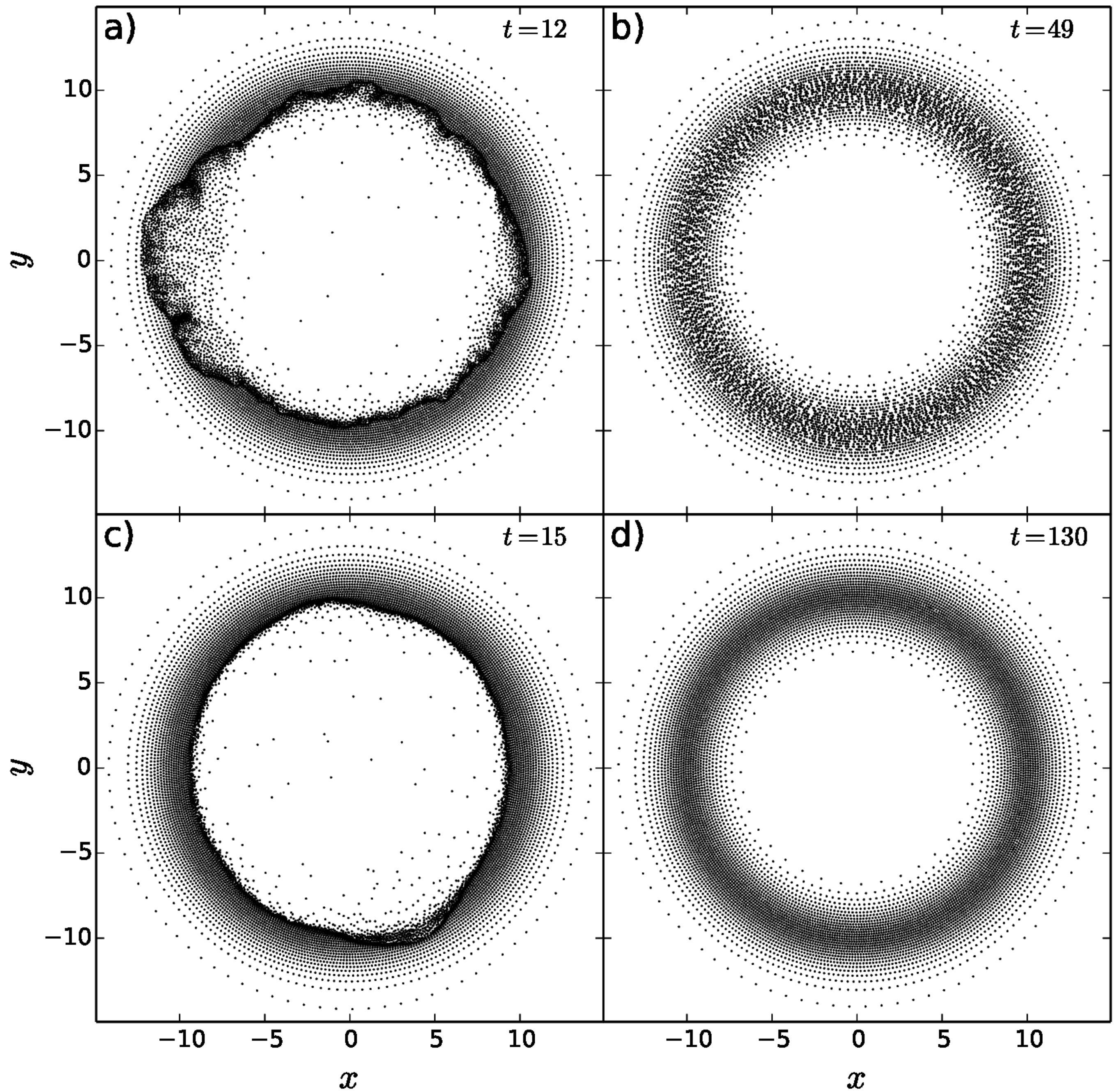

Figure 4. Particle positions for the Keplerian ring test using four different SPH schemes: (a) standard GADGET-2 with the cubic B-spline and $n = 12$ neighbors; (b) cubic B-spline with $n = 12$ and Hu et al. (2014) scheme for the artificial viscosity; (c) standard artificial viscosity and Wendland C^4 function with $n = 120$; and (d) modified GADGET-2 code with Hu et al. (2014) artificial viscosity and Wendland C^4 function with $n = 120$. Only for this last scheme the ring preserves its initial configuration and remains stable.

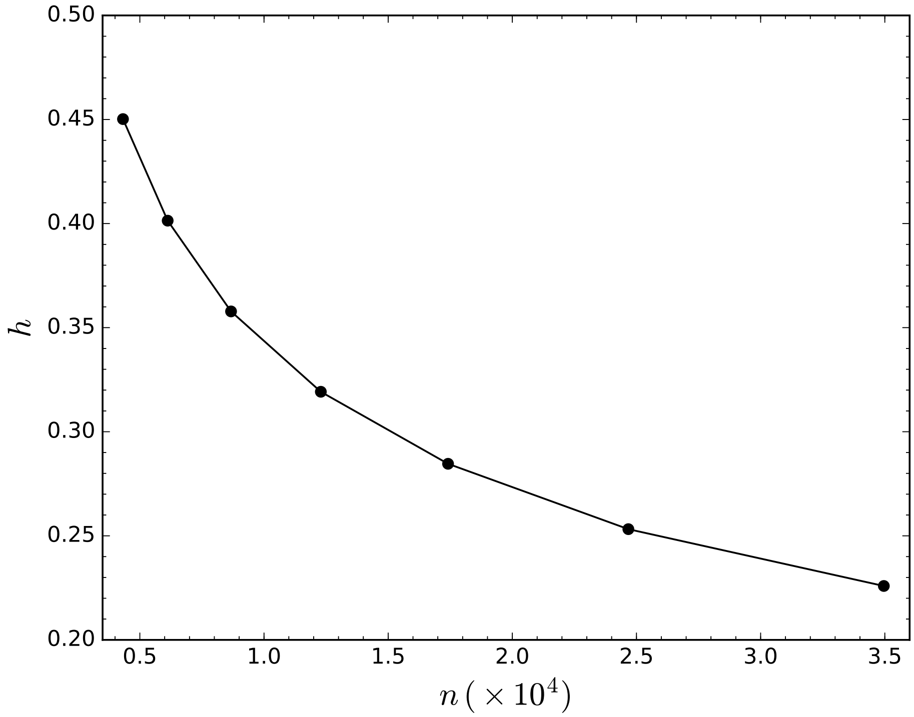

Figure 5. Variation of the smoothing length, h, with the number of neighbors, n, according to the scaling relation $h \approx 7.23n^{-0.33}$. The dots on the curve mark the values of n used for the collapse calculations of Table 2 with the C^4 Wendland function.

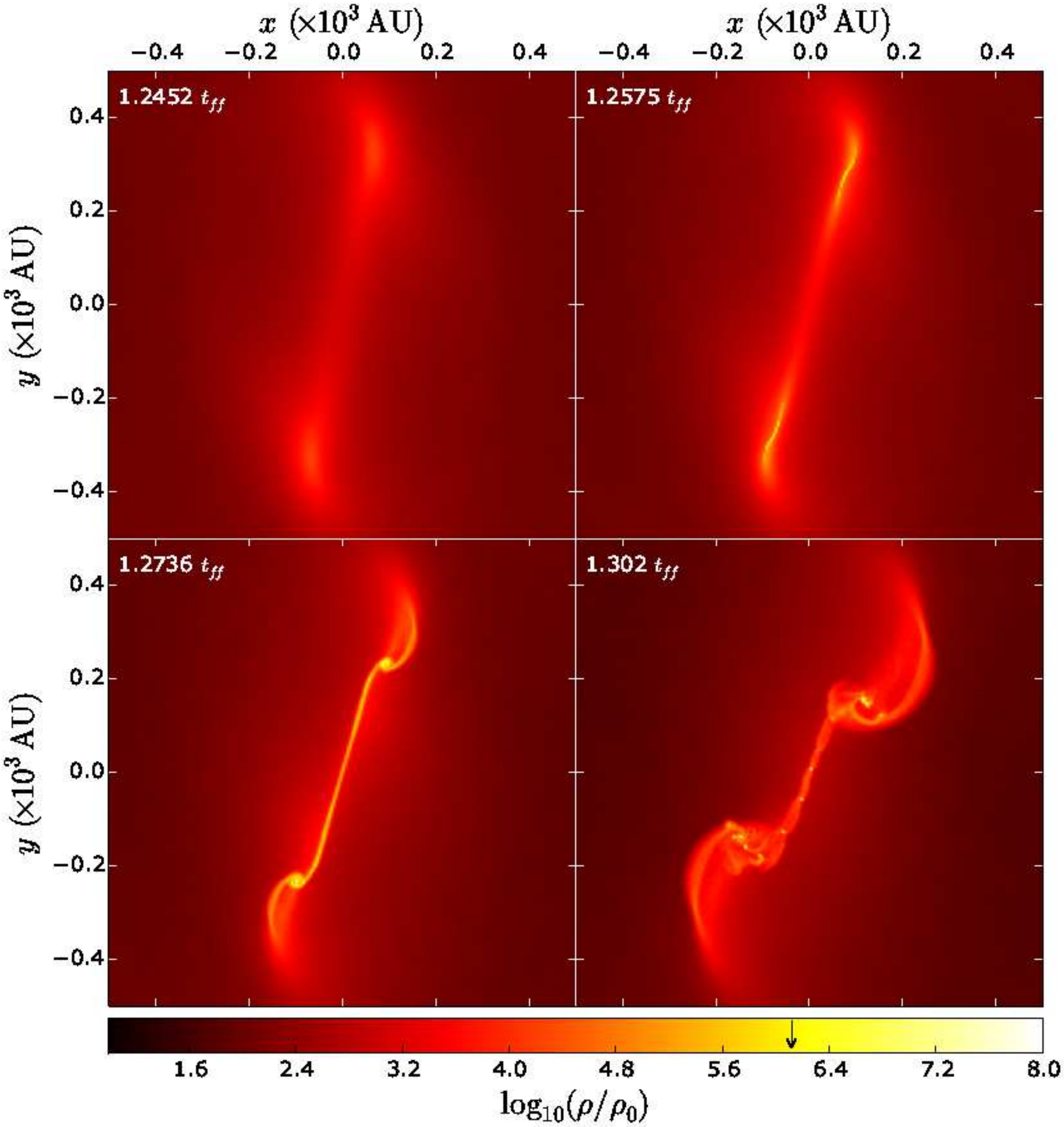

Figure 6. Density maps of the cloud center in the equatorial plane for model U4C. Four different times are shown: $t = 1.2452t_{\rm ff}$ ($\rho_{\rm max} \approx 10^{4.22}\rho_0$), $t = 1.2575t_{\rm ff}$ ($\rho_{\rm max} \approx 10^{6.97}\rho_0$), $t = 1.2736t_{\rm ff}$ ($\rho_{\rm max} \approx 10^{8.91}\rho_0$), and $t = 1.302t_{\rm ff}$ ($\rho_{\rm max} \approx 10^{9.74}\rho_0$). The color bar at the bottom shows the logarithm of the density normalized to the initial value ρ_0 and the vertical arrow marks the critical density beyond which the collapse becomes adiabatic.

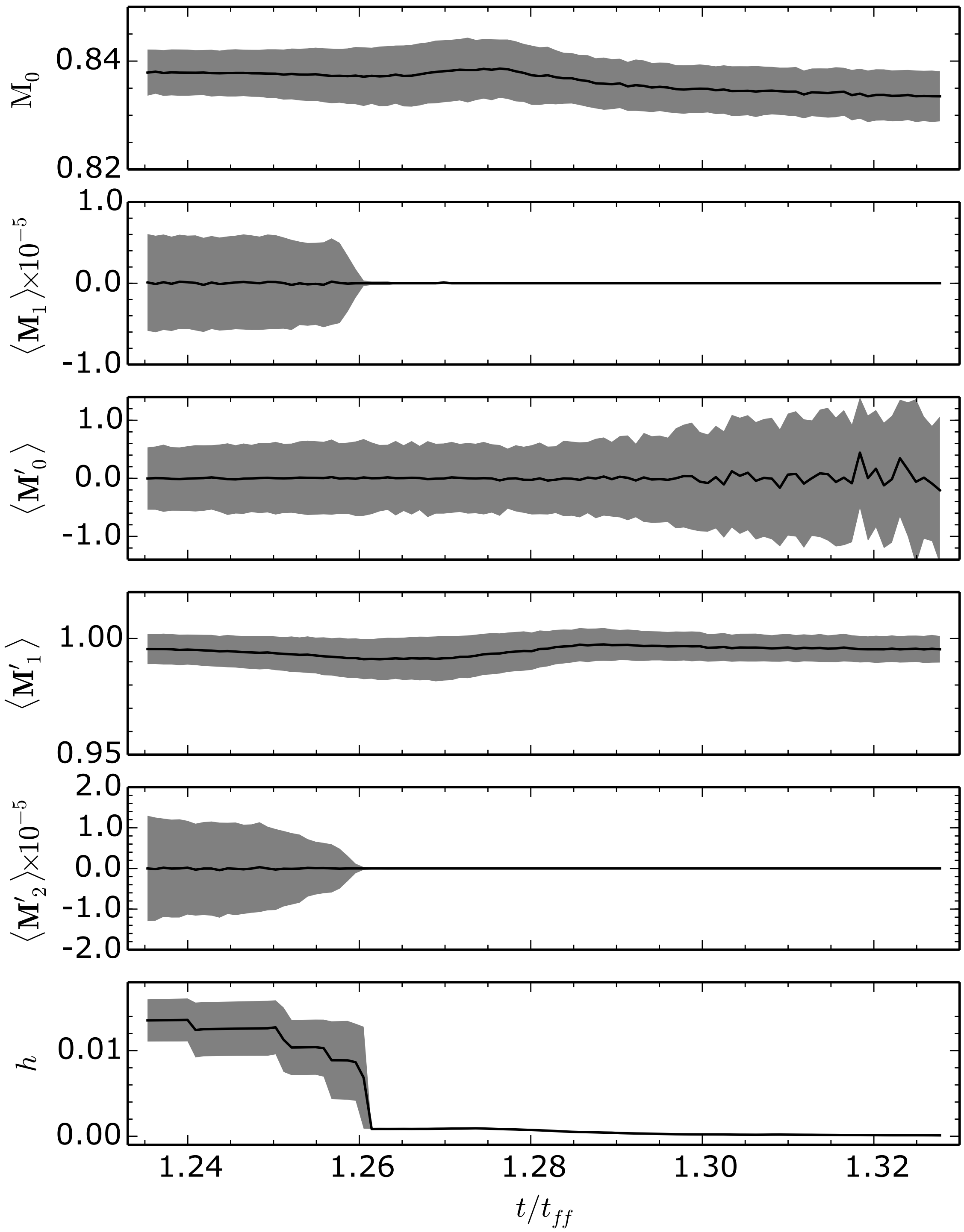

Figure 7. Time evolution of the discrete first moments (18)–(21) and smoothing length for the last stages of collapse of model U4C. The solid line in each plot represents the maximum of the distribution for each quantity where most particles lie, while the gray strips around the maximum correspond to distributions composed of much lower numbers of particles. Bracketed quantities have the same meaning as in Figures 2 and 3.

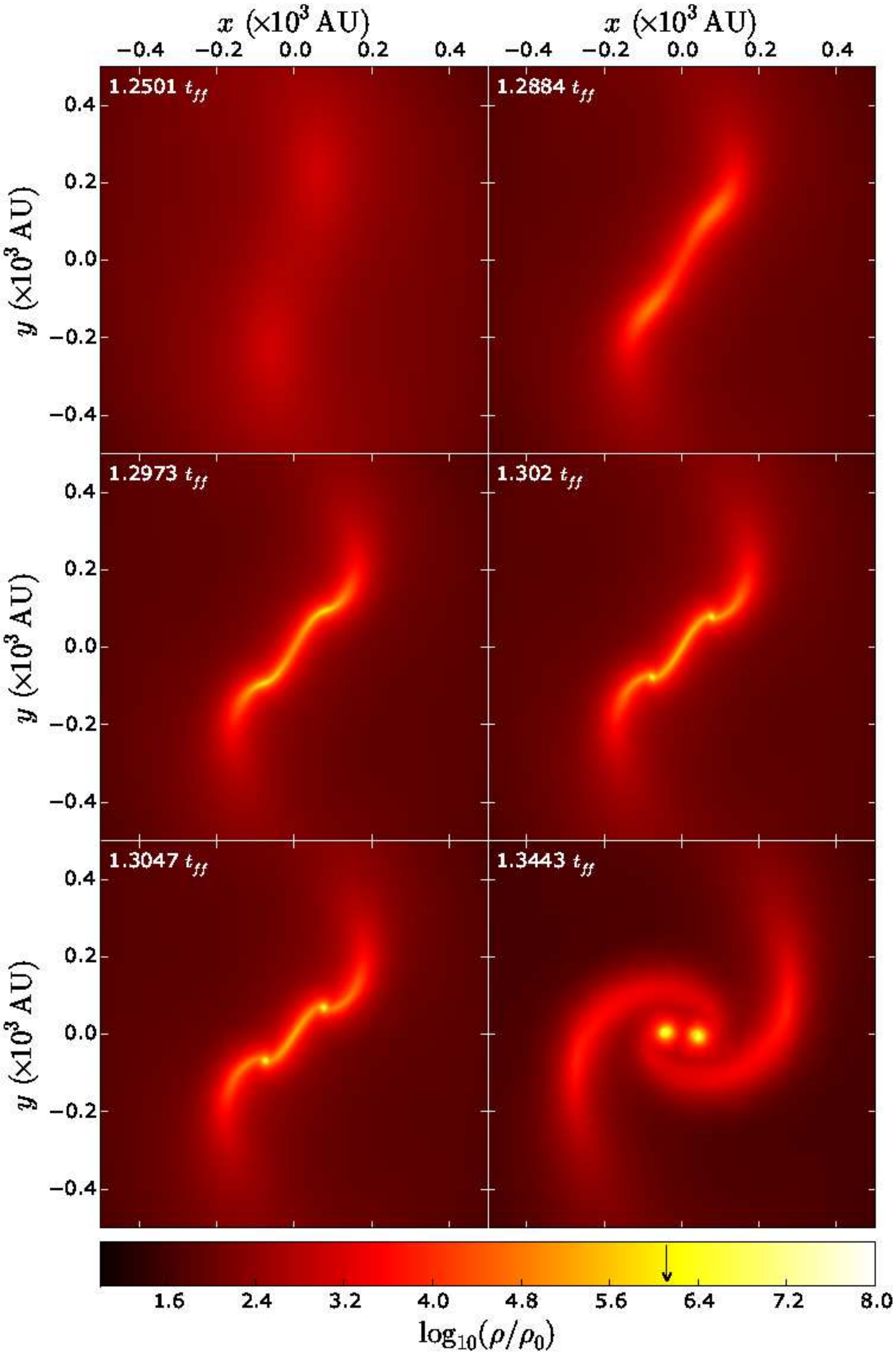

Figure 8. Density maps of the cloud center in the equatorial plane for model U2W. Six different times are shown: $t = 1.2501t_{\rm ff}$ ($\rho_{\rm max} \approx 10^{3.05}\rho_0$), $t = 1.2884t_{\rm ff}$ ($\rho_{\rm max} \approx 10^{4.84}\rho_0$), $t = 1.2973t_{\rm ff}$ ($\rho_{\rm max} \approx 10^{6.75}\rho_0$), $t = 1.302t_{\rm ff}$ ($\rho_{\rm max} \approx 10^{8.43}\rho_0$), $t = 1.3047t_{\rm ff}$ ($\rho_{\rm max} \approx 10^{8.64}\rho_0$), and $t = 1.3443t_{\rm ff}$ ($\rho_{\rm max} \approx 10^{9.47}\rho_0$). The color bar at the bottom shows the logarithm of the density normalized to the initial value ρ_0 and the vertical arrow marks the critical density beyond which the collapse becomes adiabatic.

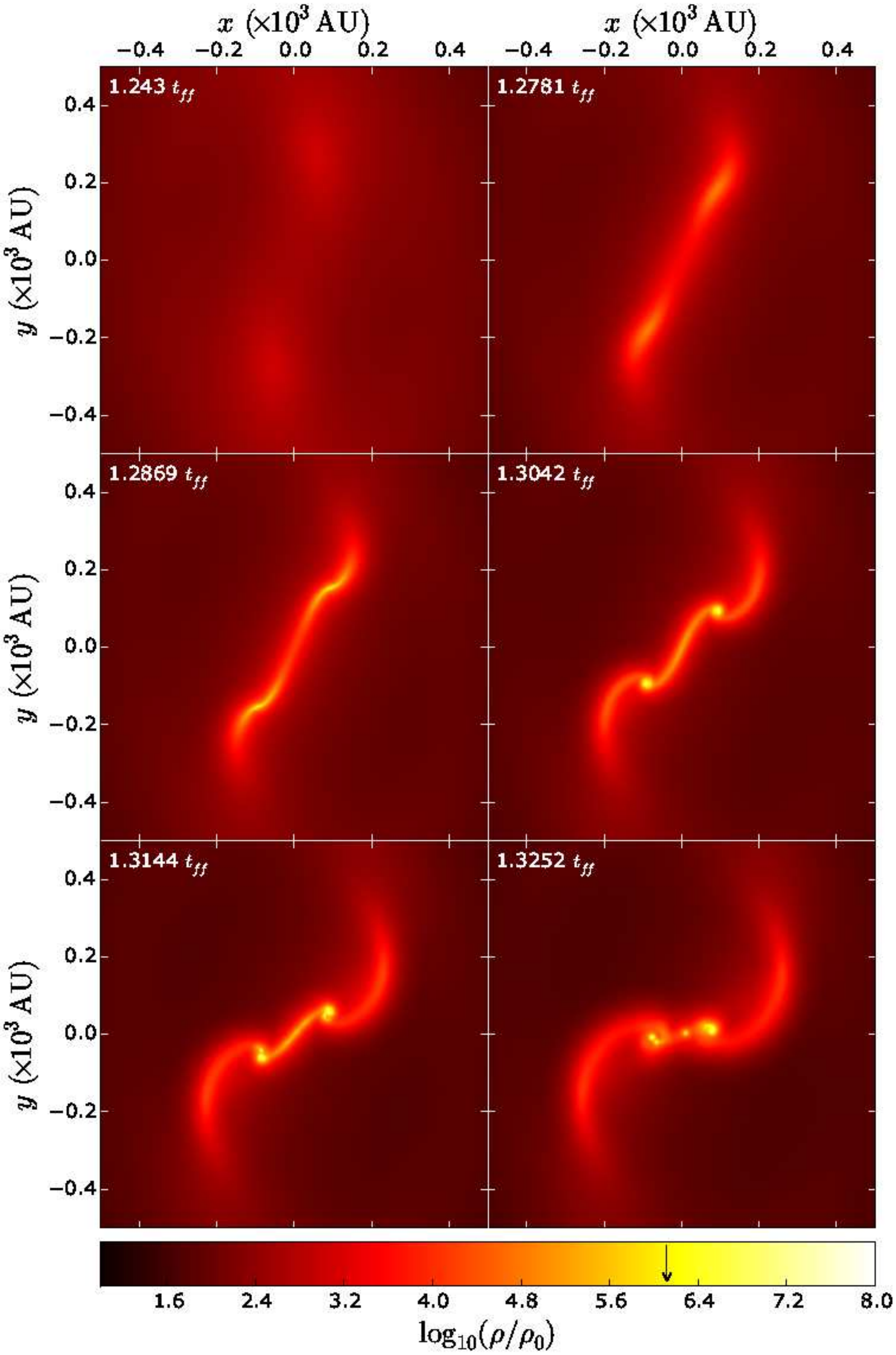

Figure 9. Density maps of the cloud center in the equatorial plane for model U4W. Six different times are shown: $t = 1.243t_{\rm ff}$ ($\rho_{\rm max} \approx 10^{3.0}\rho_0$), $t = 1.2781t_{\rm ff}$ ($\rho_{\rm max} \approx 10^{4.84}\rho_0$), $t = 1.2869t_{\rm ff}$ ($\rho_{\rm max} \approx 10^{6.75}\rho_0$), $t = 1.3042t_{\rm ff}$ ($\rho_{\rm max} \approx 10^{8.43}\rho_0$), $t = 1.3144t_{\rm ff}$ ($\rho_{\rm max} \approx 10^{8.62}\rho_0$), and $t = 1.3252t_{\rm ff}$ ($\rho_{\rm max} \approx 10^{9.46}\rho_0$). The color bar at the bottom shows the logarithm of the density normalized to the initial value ρ_0 and the vertical arrow marks the critical density beyond which the collapse becomes adiabatic.

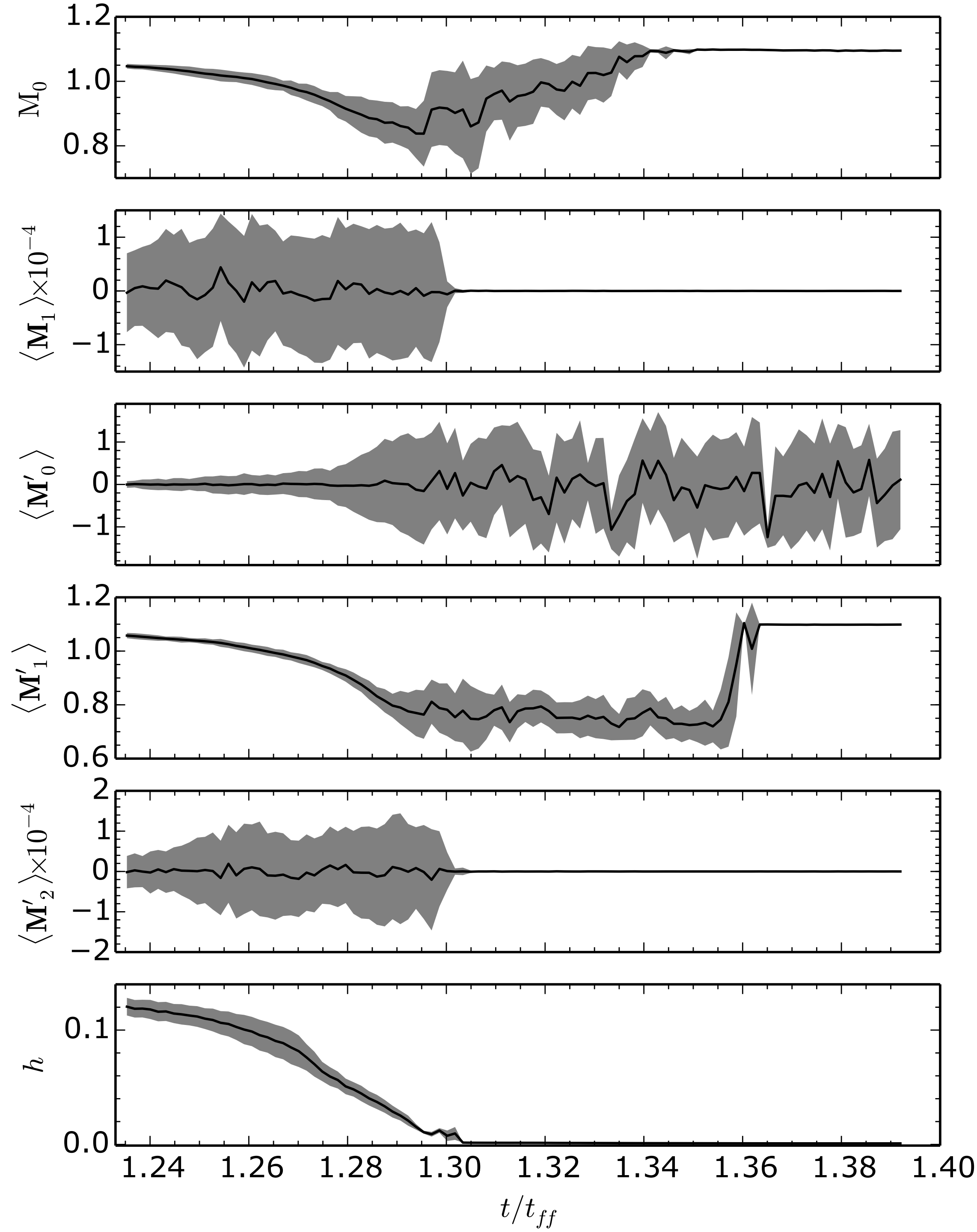

Figure 10. Time evolution of the discrete first moments (18)–(21) and smoothing length for the last stages of collapse of model U2W. The solid line in each plot represents the maximum of the distribution for each quantity where most particles lie, while the gray strips around the maximum correspond to distributions composed of much lower numbers of particles. Bracketed quantities have the same meaning as in Figures 2 and 3.

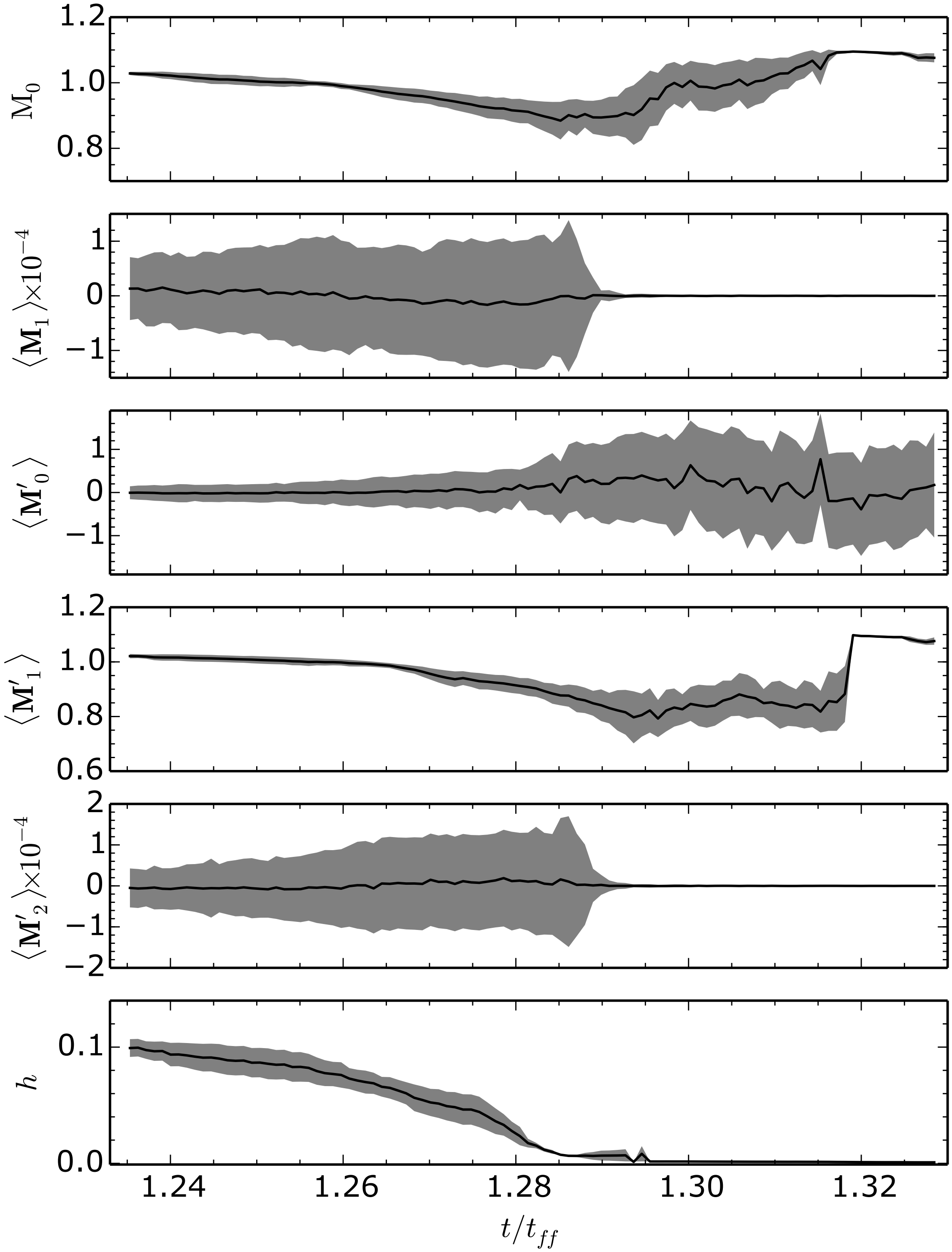

Figure 11. Time evolution of the discrete first moments (18)–(21) and smoothing length for the last stages of collapse of model U4W. The solid line in each plot represents the maximum of the distribution for each quantity where most particles lie, while the gray strips around the maximum correspond to distributions composed of much lower numbers of particles. Bracketed quantities have the same meaning as in Figures 2 and 3.

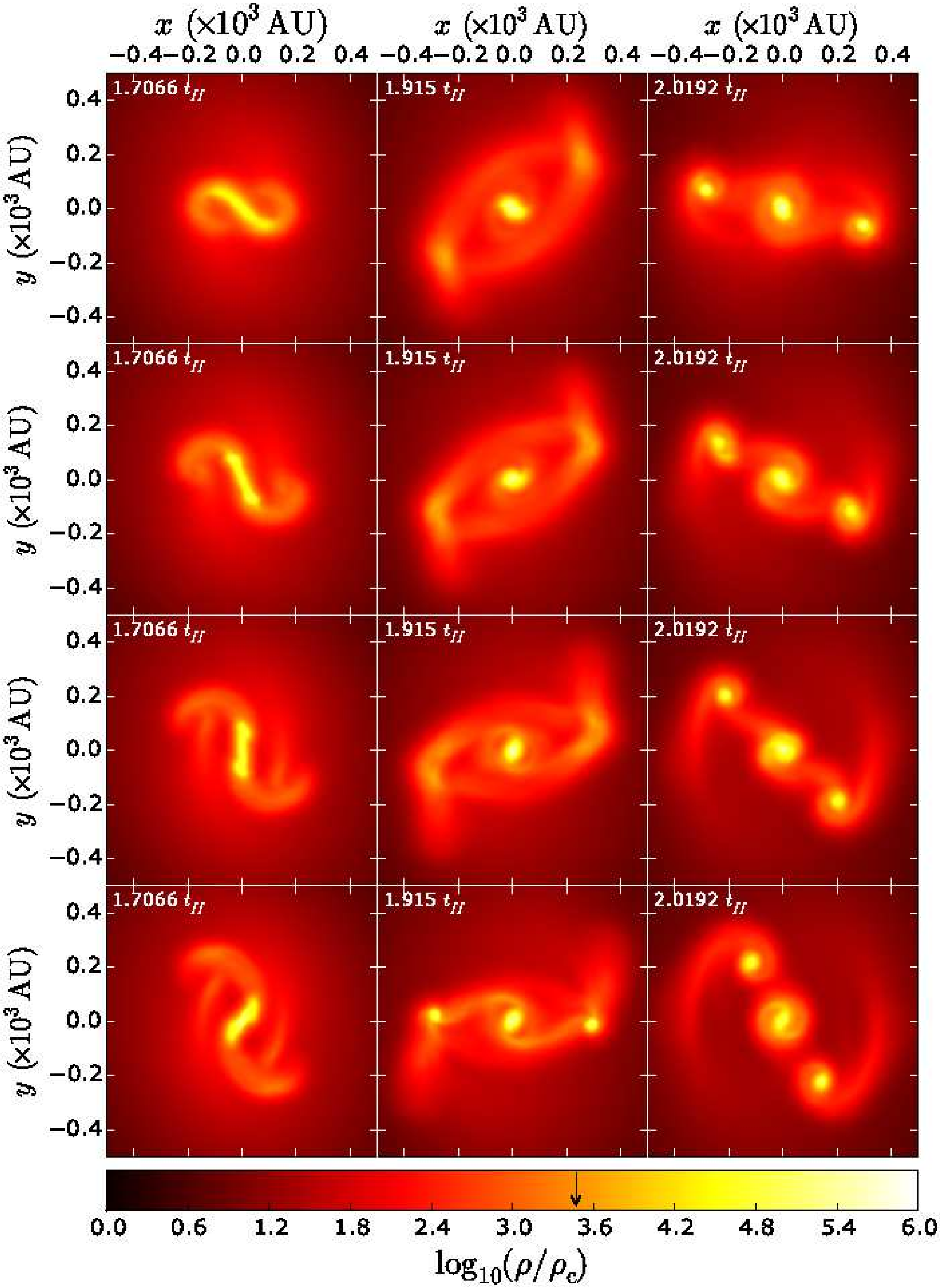

Figure 12. Density maps of the cloud center in the equatorial plane for models G3W (first row, $N = 1200000$), G4W (second row, $N = 2400000$), G5W (third row, $N = 4800000$), and G6W (last row, $N = 9600000$). Three different times are displayed for each model from left to right showing the intermediate and final stages of collapse. At $1.7066t_{\rm ff}$, $\rho_{\rm max} \approx 10^{4.70}\rho_{\rm c}$ (G3W), $\approx 10^{5.07}\rho_{\rm c}$ (G4W), $\approx 10^{5.07}\rho_{\rm c}$ (G5W), and $\approx 10^{5.35}\rho_{\rm c}$ (G6W); at $1.915t_{\rm ff}$, $\rho_{\rm max} \approx 10^{5.42}\rho_{\rm c}$ (G3W), $\approx 10^{5.41}\rho_{\rm c}$ (G4W), $\approx 10^{5.57}\rho_{\rm c}$ (G5W), and $\approx 10^{5.54}\rho_{\rm c}$ (G6W); and at $2.0192_{\rm ff}$, $\rho_{\rm max} \approx 10^{5.58}\rho_{\rm c}$ (G3W), $\approx 10^{5.39}\rho_{\rm c}$ (G4W), $\approx 10^{5.44}\rho_{\rm c}$ (G5W), and $\approx 10^{5.32}\rho_{\rm c}$ (G6W), where $\rho_{\rm c} = 1.7 \times 10^{-17}$ g cm^{-3} is the initial central density. The color bar at the bottom shows the logarithm of the density normalized to $\rho_{\rm c}$ and the vertical arrow marks the critical density beyond which the collapse becomes adiabatic.

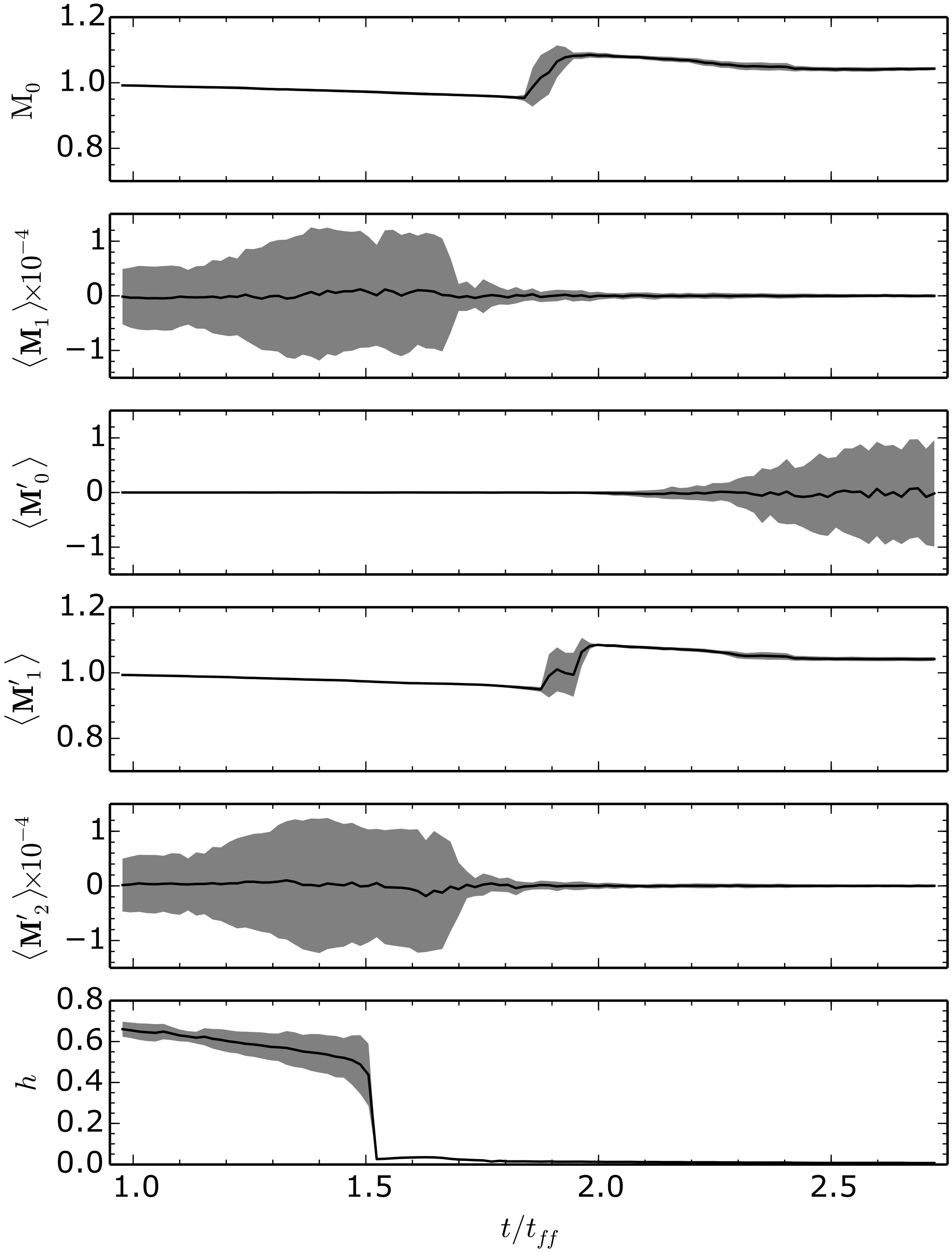

Figure 13. Time evolution of the discrete first moments (18)–(21) and smoothing length for the last stages of collapse of model G3W. The solid line in each plot represents the maximum of the distribution for each quantity where most particles lie, while the gray strips around the maximum correspond to distributions composed of much lower numbers of particles. Bracketed quantities have the same meaning as in Figures 2 and 3.

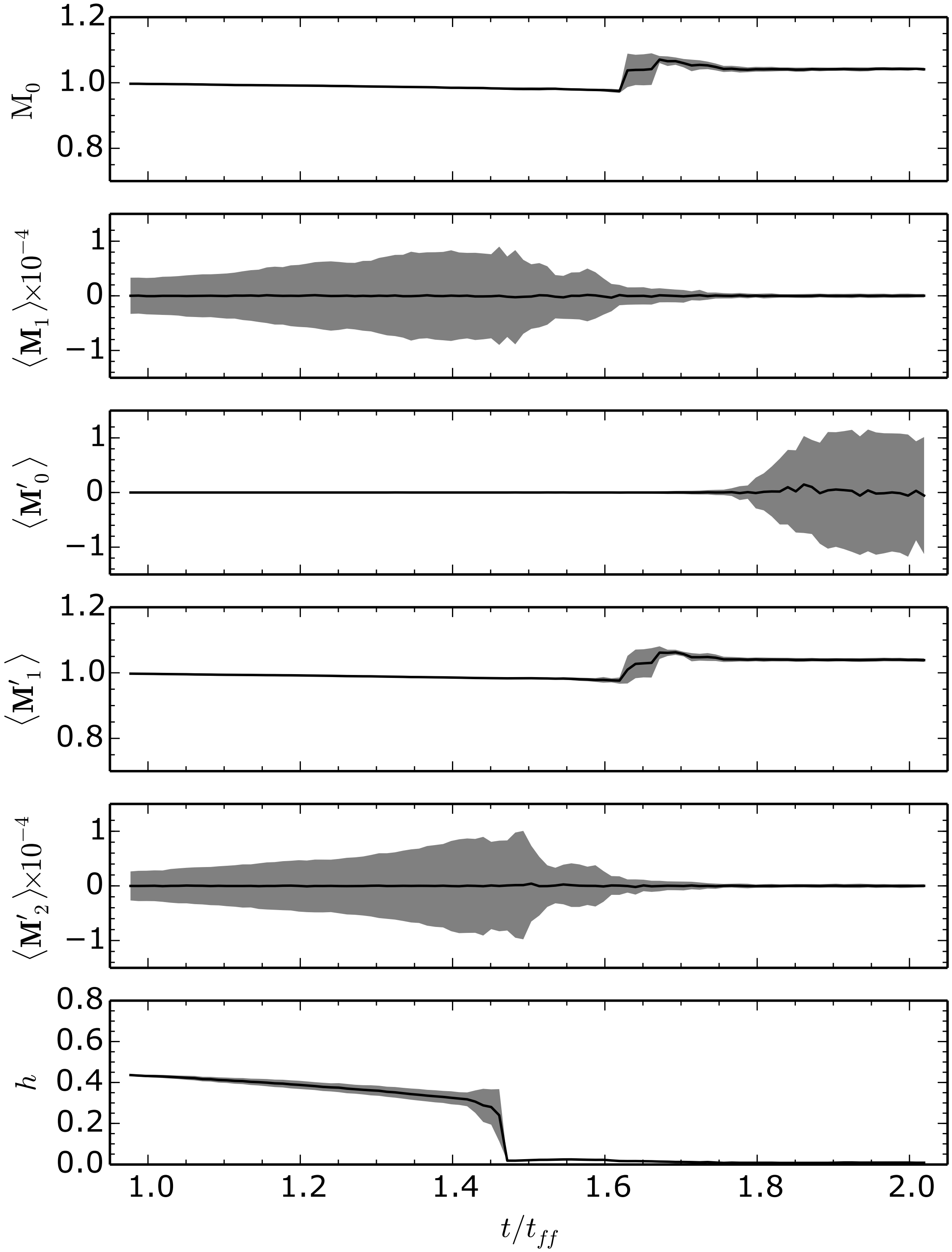

Figure 14. Time evolution of the discrete first moments (18)–(21) and smoothing length for the last stages of collapse of model G6W. The solid line in each plot represents the maximum of the distribution for each quantity where most particles lie, while the gray strips around the maximum correspond to distributions composed of much lower numbers of particles. Bracketed quantities have the same meaning as in Figures 2 and 3.

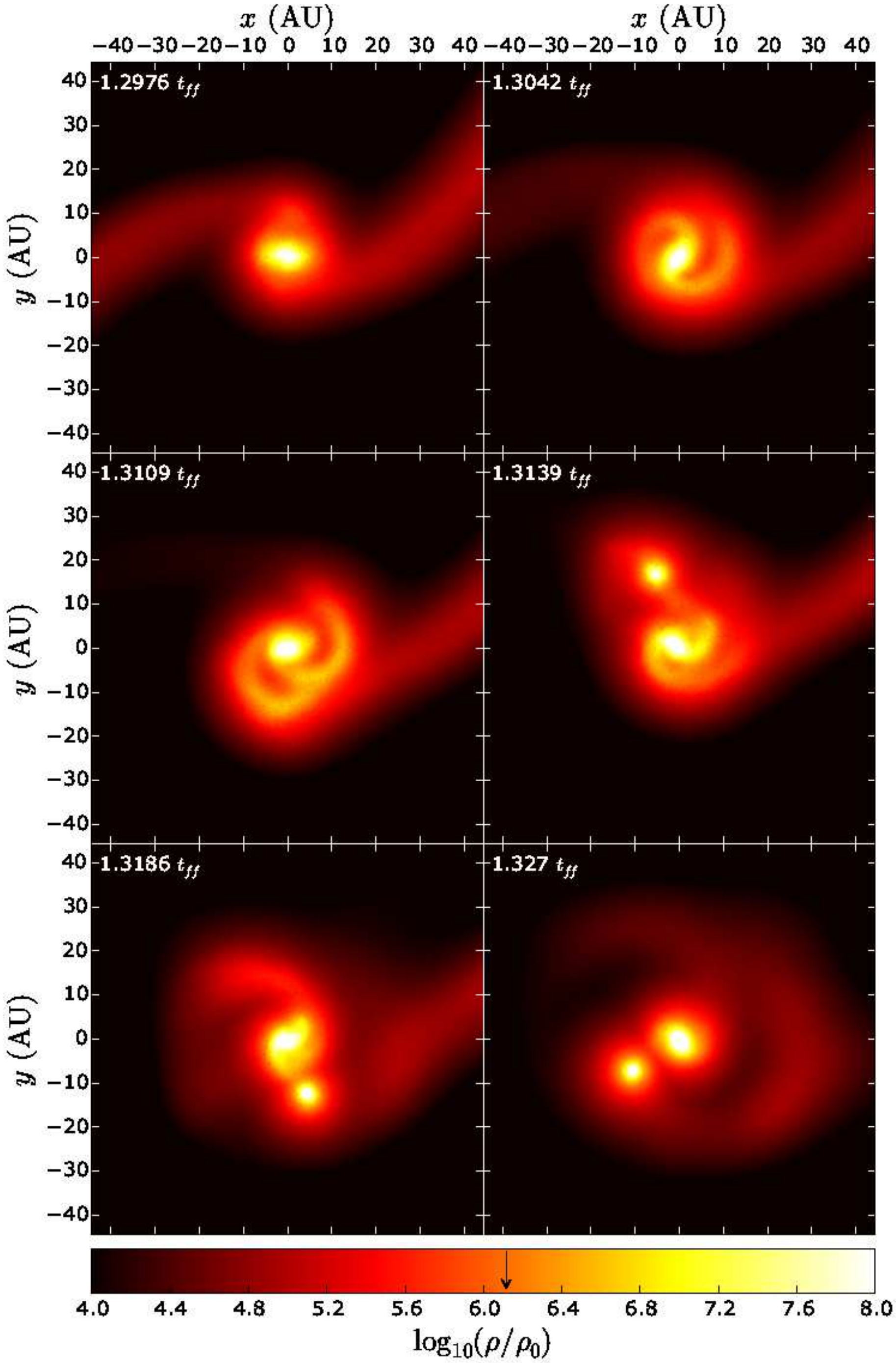

Figure 15. Enlarged density maps in the equatorial plane of one of the binary protostars that formed in model U4W. Six different times are shown: $t = 1.2976t_{\rm ff}$ ($\rho_{\rm max} \approx 10^{8.23}\rho_0$), $t = 1.3042t_{\rm ff}$ ($\rho_{\rm max} \approx 10^{8.42}\rho_0$), $t = 1.3109t_{\rm ff}$ ($\rho_{\rm max} \approx 10^{8.53}\rho_0$), $t = 1.3139t_{\rm ff}$ ($\rho_{\rm max} \approx 10^{8.64}\rho_0$), $t = 1.3186t_{\rm ff}$ ($\rho_{\rm max} \approx 10^{8.89}\rho_0$), $t = 1.3270t_{\rm ff}$ ($\rho_{\rm max} \approx 10^{9.77}\rho_0$). A close binary of maximum orbital separation ≈ 20 AU is formed by fragmentation of the gravitationally unstable disk around the primary. The color bar at the bottom shows the logarithm of the density normalized to the initial value ρ_0 and the vertical arrow marks the critical density beyond which the collapse becomes adiabatic.